



LJMU Research Online

Brivio, R, Campana, S, Covino, S, Ferro, M, Gianfagna, G, Bernardini, MG, D'Avanzo, P, Giarratana, S, Ghirlanda, G, Hu, YD, Melandri, A, Nava, L, Piro, L, Rossi, A, Salafia, OS, Salvaggio, C, Salvaterra, R, Sbarrato, T, Sbarufatti, B, Tagliaferri, G, Thakur, AL, Tovmassian, G, Agüí Fernández, JF, Bruni, G, Castro-Tirado, AJ, Delia, V, De Pasquale, M, De Ugarte Postigo, A, De Wet, S, Hartmann, DH, Klose, S, Kobayashi, S, Maiorano, E, Malesani, DB, Marini, E, Martin-Carrillo, A, Nicuesa Guelbenzu, A, Pandey, SB, Paris, D, Pugliese, G, Rau, A, Ricci, R, Saccardi, A, Sánchez-Ramírez, R, Tanvir, NR, Thöne, CC and Zafar, T

A comprehensive broadband analysis of the high-redshift GRB 240218A

<http://researchonline.ljmu.ac.uk/id/eprint/26273/>

Article

Citation (please note it is advisable to refer to the publisher's version if you intend to cite from this work)

Brivio, R, Campana, S, Covino, S, Ferro, M, Gianfagna, G, Bernardini, MG, D'Avanzo, P, Giarratana, S, Ghirlanda, G, Hu, YD, Melandri, A, Nava, L, Piro, L, Rossi, A, Salafia, OS, Salvaggio, C, Salvaterra, R, Sbarrato, T, Sbarufatti, B, Tagliaferri, G, Thakur, AL, Tovmassian, G, Agüí Fernández, JF, Bruni, G.

LJMU has developed **LJMU Research Online** for users to access the research output of the University more effectively. Copyright © and Moral Rights for the papers on this site are retained by the individual authors and/or other copyright owners. Users may download and/or print one copy of any article(s) in LJMU Research Online to facilitate their private study or for non-commercial research. You may not engage in further distribution of the material or use it for any profit-making activities or any commercial gain.

<http://researchonline.ljmu.ac.uk/>

The version presented here may differ from the published version or from the version of the record. Please see the repository URL above for details on accessing the published version and note that access may require a subscription.

For more information please contact researchonline@ljmu.ac.uk

A comprehensive broadband analysis of the high-redshift GRB 240218A

R. Brivio^{1,2,*}, S. Campana¹, S. Covino^{1,3}, M. Ferro^{1,2}, G. Gianfagna⁴, M. G. Bernardini¹, P. D'Avanzo¹, S. Giarratana¹, G. Ghirlanda¹, Y.-D. Hu^{5,1}, A. Melandri⁶, L. Nava¹, L. Piro⁴, A. Rossi⁷, O. S. Salafia¹, C. Salvaggio¹, R. Salvaterra⁸, T. Sbarrato¹, B. Sbarufatti¹, G. Tagliaferri¹, A. L. Thakur⁴, G. Tovmassian^{1,9}, J.F. Agüí Fernández¹⁰, G. Bruni⁴, A. J. Castro-Tirado^{11,12}, V. D'Elia^{13,6}, M. De Pasquale¹⁴, A. de Ugarte Postigo^{15,16}, S. de Wet¹⁷, D. H. Hartmann¹⁸, S. Klose¹⁹, S. Kobayashi²⁰, E. Maiorano⁷, D. B. Malesani^{21,22,23}, E. Marini⁶, A. Martin-Carrillo²⁴, A. Nicuesa Guelbenzu¹⁹, S. B. Pandey²⁵, D. Paris⁶, G. Pugliese²⁶, A. Rau²⁷, R. Ricci^{28,29}, A. Saccardi³⁰, R. Sánchez-Ramírez¹¹, N. R. Tanvir³¹, C. C. Thöne³², and T. Zafar³³

(Affiliations can be found after the references)

Received 25 October 2024 / Accepted 18 February 2025

ABSTRACT

Context. The detection and follow-up observations of high-redshift ($z > 6$) gamma-ray bursts (GRBs) provide a unique opportunity to explore the properties of the distant Universe. Unfortunately, they are rather rare, with only a dozen of them identified so far.

Aims. We present here the discovery of the GRB with the second highest spectroscopic redshift measured to date, GRB 240218A at $z = 6.782$, and the broadband analysis of its afterglow. Following the detection by high-energy satellites, we obtained multi-epoch and multi-wavelength photometric follow-up observations, from 68 s to ~ 48 d after the detection. These data allow us to perform a comprehensive study of the emission and physical properties of this event. We also compare these properties with GRBs observed at high and low redshift.

Methods. We built the X-ray, near-infrared, and radio light curves and studied their temporal evolution. Moreover, we investigated the spectral energy distribution (SED) at different times to trace possible spectral evolution. We also compared the prompt phase properties, X-ray luminosity, and optical extinction of GRB 240218A with those of the long-duration GRB (LGRB) population.

Results. The SED analysis reveals a typical afterglow-like behaviour at late times. The origin of the early-time emission is uncertain, with the probable presence of an additional contribution on top of the afterglow emission. From the broadband physical modelling of the afterglow, we identify a narrow Gaussian jet seen slightly off-axis, $\theta_v = 2.52^{+0.57}_{-0.29}$ deg, and pinpoint the presence of a possible jet break ~ 0.86 d after the trigger.

Conclusions. The results of the analysis and the comparison with other high- z GRBs reveal that we can consider GRB 240218A as a 'standard' high-redshift LGRB: the prompt phase properties, the X-ray luminosity, and the optical extinction are consistent with the values derived for the LGRB population. The jet opening angle is narrower but compatible with those of high- z bursts, possibly pointing to more collimated jets at high redshift.

Key words. gamma-ray burst: general – gamma-ray burst: individual: GRB240218A

1. Introduction

The investigation of the early Universe is one of the most interesting, yet challenging, tasks in modern astrophysics. Long-duration gamma-ray bursts (LGRBs) provide an optimal tool to explore it since they are potentially detectable up to $z \sim 10$ (Cucchiara et al. 2011) or even at $z > 10$ (see, e.g. Gou et al. 2004; Kann et al. 2024). It has been established that the large majority of LGRBs are powered by the collapse of massive stars, associated with type-Ic broad-line (BL) supernovae (SNe), and intimately linked to the young stellar populations in their host galaxies (see, e.g. Hjorth et al. 2003; Fruchter et al. 2006; Woosley & Bloom 2006; Hjorth & Bloom 2012; Cano et al. 2017; Corsi & Lazzati 2021). The observation and investigation of high-redshift bursts could give us hints about the formation of the first stars, the ionisation of the early Universe and its metal enrichment history, and the properties of distant galaxies that cannot be studied with standard techniques such as direct imaging or spectroscopy. In particular,

high- z gamma-ray bursts (GRBs) provide an effective probe for investigating the evolution of the star formation rate (SFR) across cosmic time (Kistler et al. 2008; Robertson & Ellis 2012; Jakobsson et al. 2012; Matsumoto et al. 2024) and the effects of metallicity on the type-Ic BL SNe and GRB progenitors (Grieco et al. 2012). The cosmic SFR is expected to receive a larger contribution from population III (Pop III) stars at larger redshift than from nearby Pop I/II stars. The former probably played a role in the occurrence of LGRBs in the early Universe (e.g. Salvaterra 2015) if we assume that Pop III massive stars can be the progenitors of long GRBs in such environments (see, e.g. Mészáros & Rees 2010; Suwa & Ioka 2011). The early galaxies and the reionisation of the young Universe can be explored thanks to afterglow spectroscopy, which has been proven to be the cornerstone in the study of events at such high redshifts (e.g. Saccardi et al. 2023).

The discovery of new distant events is thus of the utmost importance. However, to date, fewer than $\sim 1\%$ of GRBs with a well-constrained spectroscopic redshift have been found at $z \gtrsim 6$, and all of them belong to the LGRB class: GRB 050904 ($z = 6.295$; Tagliaferri et al. 2005; Kawai et al. 2006),

* Corresponding author; riccardo.brivio@inaf.it

GRB 080913 ($z = 6.733$; Greiner et al. 2009; Patel et al. 2010), GRB 090423A ($z = 8.23$; Salvaterra et al. 2009; Tanvir et al. 2009), GRB 130606A¹ ($z = 5.913$; Chornock et al. 2013; Hartoog et al. 2015), GRB 140515A ($z = 6.327$; Melandri et al. 2015), and GRB 210905A ($z = 6.312$; Rossi et al. 2022; Saccardi et al. 2023). Other high-redshift GRBs have been discovered, but only a photometric redshift has been derived, or a low signal-to-noise spectrum was available: GRB 090429B ($z_{\text{ph}} \approx 9.4$; Cucchiara et al. 2011), GRB 100905A ($z_{\text{ph}} \approx 7.88$; Bolmer et al. 2018), GRB 120521C ($z_{\text{ph}} \approx 6$; Laskar et al. 2014), and GRB 120923A ($z \approx 7.8$; Tanvir et al. 2018).

Despite the small sample of high- z events, it is still possible to study their properties and compare them with the population of bursts at lower redshift. The detection of events at very large distances increases the robustness of the prompt and afterglow rest-frame correlations, with most of the LGRBs following the $E_{\text{peak}} - E_{\text{iso}}$ ('Amati' relation; Amati et al. 2002) and $E_{\text{peak}} - L_{\text{iso}}$ ('Yonetoku' relation; Yonetoku et al. 2004) prompt emission correlations regardless of their distance. This suggests that the prompt phase properties are intrinsic in the GRBs and not biased by their redshift measurement. Besides, the X-ray afterglow luminosity of high- z GRBs is consistent with the rest of the LGRB population (Salvaterra 2015), pointing to a common mechanism powering the afterglow emission across all redshifts. High- z bursts have also been found to consistently show a negligible rest-frame optical extinction with the majority of LGRBs (see Melandri et al. 2015; Zafar et al. 2018), while a possible evolution of the rest-frame hydrogen-equivalent column density, N_H , has been suggested (Watson et al. 2013). However, this may be ascribed to the absorption from intervening systems and the diffuse intergalactic medium along the line of sight (Campana et al. 2010, 2012). Due to temporal dilation, very high-redshift events are also optimal candidates for the study of early afterglow light curves, which can display a wide variety of behaviours, from the X-rays to the infrared (IR), and encode crucial information about the physics of the ejecta, such as the Lorentz factor of the initial fireball (Molinari et al. 2007). The geometry of GRB jets can be investigated as well, with some hints of more collimated jets at high redshift rather than at lower z (for example, see Laskar et al. 2014, 2018; Lloyd-Ronning et al. 2019, 2020a). Such an anti-correlation between the jet opening angle, θ_{jet} , and the redshift has significant implications for the properties of high-redshift GRB progenitors and their evolution over cosmic time. Narrow jets could originate from massive stars with compact envelopes and low metallicity (Woosley & Heger 2006; Sanyal et al. 2017), which were found to be more common at large redshifts (see e.g. Bromm et al. 2009; Toma et al. 2016). This in turn implies that the typical progenitor mass evolves with time, potentially indicating a top-heavier initial mass function (IMF) at higher z (e.g. van Dokkum & van der Marel 2007; Davé 2008; Leja et al. 2020). In addition, time-evolving progenitors also impact the GRB production rate and the SFR estimates at large distances (Lloyd-Ronning et al. 2020b). On the other hand, selection effects may play a role in favouring the observations of jets with smaller θ_{jet} , but Lloyd-Ronning et al. (2020a) demonstrated that even after accounting for them, the $\theta_{\text{jet}} - z$ correlation remains statistically significant, suggesting that it reflects an intrinsic property of GRB progenitors and their evolution over cosmic time.

Here, we present the discovery, observations, and analysis of GRB 240218A, which is the LGRB with the second largest spec-

troscopic redshift discovered to date, $z = 6.782$ (Saccardi et al. 2024). After the initial discovery by the *Neil Gehrels Swift* Observatory (hereafter *Swift*; Gehrels et al. 2004) and the *Fermi* Gamma-ray Space Telescope telescope, it was observed with several instruments on the ground, allowing for the determination of a multi-band and multi-epoch light curve. In this work, we analyse the X-rays, near-infrared (NIR), and radio light curves in detail, as well as the broadband spectral energy distribution (SED) at different epochs. We also compare its properties with other high- z GRBs discovered to date and with the population of LGRBs at lower distances.

The paper is organised as follows. In Sect. 2, we present the broadband observations of GRB 240218A, from the gamma-rays to the radio band, and in Sect. 3 we describe the analysis of such data. In Sect. 4, we discuss the results, while our conclusions are summarised in Sect. 5.

We adopt the Λ CDM model with cosmological parameters of $\Omega_M = 0.308$, $\Omega_\Lambda = 0.692$, and $H_0 = 67.8 \text{ km s}^{-1} \text{ Mpc}^{-1}$ (Planck Collaboration XIII 2016). All magnitudes presented in this work are given in the AB system. Errors are at a 1σ confidence level (c.l.) and upper limits at a 3σ level, unless stated otherwise. For the flux density, we adopt the convention $F_\nu(t) \propto t^\alpha \nu^\beta$.

2. Observations

2.1. Prompt phase

GRB 240218A was detected by the *Swift* Burst Alert Telescope (BAT; Barthelmy et al. 2005) on February 18 2024 at $t_0 = 02:00:00$ UT (Page et al. 2024a; Barthelmy et al. 2024), at the position (J2000) RA = 10:47:14.4, Dec = +01:17:40.2, with an uncertainty of $1.3'$ (radius, 90% c.l.). Its duration in the 15–350 keV band was $T_{90} = 66.93 \pm 11.28$ s. The mask-weighted light curve shows two major pulses separated by ~ 20 s. The peak count rate was $\sim 1400 \text{ counts s}^{-1}$ (15–350 keV) at ~ 22 s after the trigger.

GRB 240218A also triggered the Konus-Wind satellite (Svinkin et al. 2024). The Konus-Wind burst light curve shows a multi-peaked structure with the brightest peak around 20 s after the trigger, consistent with the BAT light curve. The total fluence of the burst is $7.62_{-2.22}^{+1.72} \times 10^{-6} \text{ erg cm}^{-2}$, and the peak energy flux, measured from 19.74 s, is $5.29_{-1.49}^{+2.21} \times 10^{-7} \text{ erg cm}^{-2} \text{ s}^{-1}$ (both in the 20 keV–10 MeV energy range). The time-integrated spectrum for the burst measured from $t_0 - 12.646$ s to $t_0 + 25.626$ s was modelled with a power law plus an exponential cut-off (CPL) model, $dN/dE \sim E^\gamma e^{-E(2+\gamma)/E_p}$, yielding an index $\gamma > -0.56$ and a peak energy in the spectrum $E_p = 180_{-74}^{+77}$ keV. The same CPL model applied to the spectrum near the peak count rate (measured from $t_0 + 19.738$ s to $t_0 + 25.626$ s) gives $\gamma = -1.33_{-0.29}^{+0.53}$ and $E_p = 293_{-120}^{+207}$ keV.

Moreover, the burst was detected by the *Fermi* Gamma-ray Burst Monitor (GBM) on February 18 2024 at 02:00:21.72 UT (Veres & Meegan 2024). The GBM light curve consists of a single pulse followed by weaker emission with a duration of about 38 s in the 50–300 keV band. The time-averaged spectrum from $t_0 - 2.6$ s to $t_0 + 30.2$ s is best fit by a Band function² with $E_p = 100 \pm 20$ keV, $\gamma = -0.3 \pm 0.3$, and $\beta_B = -1.9 \pm 0.1$. The fluence in this time interval in the 10–1000 keV band is $(5.2 \pm 0.4) \times 10^{-6} \text{ erg cm}^{-2}$, the 1-s peak photon flux measured starting from $t_0 + 1.5$ s is $3.1 \pm 0.2 \text{ ph cm}^{-2} \text{ s}^{-1}$.

² A Band function (Band et al. 1993) is a broken power law with low- and high-energy spectral indices γ and β_B , smoothly connected by an exponential cut-off at E_p .

¹ We include also this GRB since it lies just below the $z = 6$ threshold.

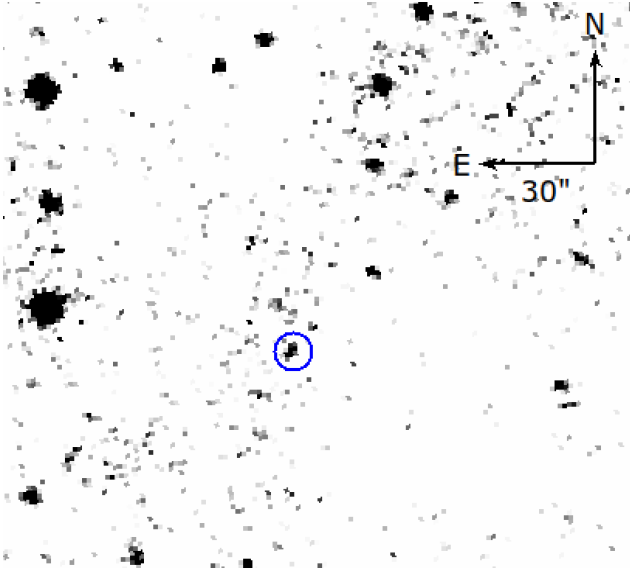


Fig. 1. Finding chart for the REM/REMIR H -band observation of GRB 240218A field taken on February 18 2024. The position of the NIR afterglow is marked with a blue circle.

2.2. Afterglow phase: X-rays

The *Swift* X-ray Telescope (XRT; Burrows et al. 2005) began observing the field at 02:02:30.1 UT, 149.4 seconds after the BAT trigger, and found a bright, uncatalogued, fading X-ray source (Evans et al. 2024; Page et al. 2024b), located at the enhanced position (J2000) RA = 10:47:11.24, Dec = +01:16:34.8, with an uncertainty of 4.2'' (radius, 90% c.l.). Follow-up observations were carried out up to ~ 3.47 days after t_0 .

The burst was also observed with the *Chandra* X-ray Observatory (CXO) beginning on March 4 2024 at 23:02:14 UT (≈ 16 days post-burst, obsID: 29317, PI Peña) for a total exposure of 20 ks (Peña et al. 2024). The source was detected with a count rate of 5.5×10^{-4} counts s^{-1} (0.3–8 keV band) at a position consistent with that of the X-ray, NIR and radio afterglow (Evans et al. 2024; D’Avanzo et al. 2024; Schroeder et al. 2024).

2.3. Afterglow phase: Optical/NIR

The NIR afterglow of GRB 240218A was discovered by the Rapid Eye Mount (REM) telescope 68 s after the *Swift* trigger (D’Avanzo et al. 2024). Following this first detection, the afterglow of GRB 240218A was observed and followed up by several telescopes, while one detection only in the optical (z band) was derived. We present here all the observations carried out in these bands. A finding chart displaying the position of the NIR afterglow is shown in Fig. 1, and the results of the observations described below are reported in Table A.1.

2.3.1. REM

We obtained optical/NIR observations with the 0.6 m robotic REM telescope (Zerbi et al. 2001; Covino et al. 2004), located at the European Southern Observatory (ESO) at La Silla (Chile). The observations started on February 18 2024 at 02:01:08 UT, which is 68 s after the burst, and continued for about 3 h with the source still visible. All the images were automatically reduced through the *jitter* script of the *eclipse* package (Devillard

1997), which aligns and stacks five individual images to obtain one average frame for each sequence, and it also performs sky subtraction. Within the *Swift*/XRT error circle, a bright NIR afterglow was detected in the H band. The coordinates of the source are (J2000) RA = 10:47:11.51, Dec = +01:16:35.09, with an uncertainty of 0.5''. Upper limits were derived for the g , r , i , and z optical bands, while the J and K filters were not available at the time of the observations.

2.3.2. MeerLICHT

Early observations of GRB 240218A were obtained with the 0.6 m wide-field MeerLICHT optical telescope (Bloemen et al. 2016) located at the South African Astronomical Observatory (SAAO) site in Sutherland, South Africa. Observations began 96 s post-trigger and continued for about 1 h, and consisted of a series of 60 s exposures in the u , g , r , i , z , and q (440–720 nm) filters following the repeating filter sequence *quqqqrqiqz*. No optical source was detected at the position of GRB 240218A in any of the individual 60 s exposures (de Wet et al. 2024). We therefore coadded the exposures in each filter to obtain deeper 3σ upper limits at a mid-time of 36 min post-trigger.

2.3.3. VLT/X-shooter

The field of GRB 240218A was observed twice with the X-shooter instrument (Vernet et al. 2011) mounted on the ESO Very Large Telescope (VLT) UT3 at the Paranal Observatory, Chile. During the first observation, around 1 h after the trigger, no afterglow candidate was detected in the optical acquisition camera, which obtained images in the g , r , and z bands (Malesani & Le Floch 2024). Following the identification of the NIR afterglow, a spectroscopic sequence was successfully obtained, revealing the presence of multiple absorption features, all at a common redshift $z = 6.782$ (Saccardi et al. 2024). The details describing the X-shooter spectral analysis can be found in Saccardi et al. (in prep.).

2.3.4. VLT/FORS2

The optical afterglow was detected with the ESO-VLT UT1 (Kueyen) equipped with the FOcal Reducer/low dispersion Spectrograph 2 (FORS2; Appenzeller et al. 1998). Our first observation was carried out at a mid-time of $t - t_0 = 2.925$ h in the z filter, following the non-detection of the afterglow in the X-shooter acquisition camera. These deeper images allowed for the detection of a new, transient source in the coadded image, for a total exposure time of 1080 s (Malesani 2024). The magnitude measured for the optical afterglow is $z = 23.8 \pm 0.15$, which was calibrated against the Pan-STARRS DR1 catalogue (Chambers et al. 2016). A further observation was performed the following night at a mid-time of $t - t_0 = 26.215$ h in the R filter. This observation was requested when the GRB redshift was not known yet, and was intended as a ‘veto’ observation (a detection in the R band would rule out $z \gtrsim 5$). Consistently with the measured redshift, no optical source was detected down to an approximate 3σ upper limit of $r = 26.3$.

2.3.5. LBT

The night after the GRB was detected, observations were taken in the J ($t_{\text{exp}} \sim 35$ min), H ($t_{\text{exp}} \sim 53$ min), and K_S ($t_{\text{exp}} \sim 87$ min) bands with the LUCI cameras mounted on

the Large Binocular Telescope (LBT) at Mount Graham, USA (Seifert et al. 2003). They started on February 19 2024 at a mid-time of 08:02:00 UT, ~ 1.3 days after the trigger. The afterglow was clearly detected in all three bands (Rossi et al. 2024).

2.3.6. TNG

Following the NIR multiple detections, additional observations were obtained with the Near Infrared Camera Spectrometer (NICS) mounted on the Telescopio Nazionale Galileo (TNG) at La Palma, Spain (Baffa et al. 2001). They were secured at mid times of $t - t_0 \sim 2.96$ and ~ 5.90 days. Data were reduced and stacked together with the `jitter` tool of the `eclipse` package to obtain a co-added frame for each epoch, and the NIR afterglow was detected at both epochs.

2.3.7. GTC

Optical observations of the GRB field were also obtained with the Optical System for Imaging and low-Intermediate-Resolution Integrated Spectroscopy (OSIRIS) mounted on the 10.4 m Gran Telescopio de Canarias (GTC) at La Palma, Spain. The observations commenced on February 19 2024 at 03:08:03 UT, approximately 1.1 days after the trigger, and were performed with the r ($t_{\text{exp}} = 360$ s), i ($t_{\text{exp}} = 400$ s), and z ($t_{\text{exp}} = 120$ s) filters. The afterglow was not detected at the burst location and upper limits were determined.

Further observations were obtained in the J , H , and K_S filters with the Espectrografo Multiobjeto Infra-Rojo (EMIR), mounted on the GTC (Garzón et al. 2022). The observations consisted of 30 min on target per band in each filter (189×10 s in J , 265×6 s in H , and 3×588 s in K_S) and had mid epochs on February 21 2024 at 03:04:38, 01:40:53, and 04:04:45 UT (3.0449, 2.9867, and 3.0866 days after the burst), respectively, and the afterglow was detected in all bands.

The data were reduced using a self-developed pipeline based on shell scripts, Python and IRAF (Tody 1986). Raw images (both science and calibration) were corrected for differential column readout level by averaging overscan pixels at the first and last rows. As a second step, we calculated the median of the twilight sky images for each filter, excluding bad pixels and star images with a sigma clipping, to create a flat field that is then normalised. All the science frames were then divided by the normalised flat field for each filter. We then calculated a sky frame for each observing cycle, by calculating the median level of the science dithered images. While creating this median frame, we excluded the highest pixels to eliminate the contribution of stars in the field. Finally, each sky frame was normalised. This normalised sky frame was multiplied by the median of each flat-fielded sky frame and the result was subtracted from it to create a science frame clean of sky background. The astrometry of the science frames was then tweaked to match the first frame by calculating an average offset of the stars in the field, using SExtractor (Bertin & Arnouts 1996) for object detection and a self-made Python code for the offset calculation and header correction. As a final step, all the science frames were combined to create the final image for each filter using Swarp (Bertin et al. 2002).

2.3.8. GROND

Additional NIR data were obtained with GROND (Gamma-Ray Burst Optical Near-Infrared Detector; Greiner et al. 2008)

mounted at the 2.2 m MPG telescope at ESO La Silla Observatory, at a common mid-time of $t - t_0 \sim 4.08$ d. The NIR counterpart was not detected in the images down to 3σ upper limits of $J > 20.0$, $H > 19.4$, and $K_S > 16.9$, calibrated against the 2MASS catalogue (Skrutskie et al. 2006). Data were reduced in a standard fashion using IRAF tasks implemented in the pipeline written to reduce GROND data (Krühler et al. 2008; Küpcü Yoldaş et al. 2008).

2.3.9. VLT/HAWK-I

Observations continued at later times with the VLT HAWK-I (High Acuity Widefield K -band Imager; Pirard et al. 2004; Kissler-Patig et al. 2008) NIR imager at Paranal Observatory, at mid times of ~ 12 and ~ 17 days after the trigger. The data were reduced using the HAWK-I pipeline under the ESOReflex environment (Freudling et al. 2013). The afterglow was detected in the first epoch, while an upper limit was obtained from the second observation.

2.4. Afterglow phase: Radio-mm

2.4.1. VLA

We performed observations with the Karl G. Jansky Very Large Array (VLA) 8.19 (February 26 2024), 18.15 (March 7 2024), and 38.08 (March 27 2024) days post-burst (PI: Giarratana; project code: SF161095) at the central frequencies of 6 (C band) and 10 GHz (X band), with a bandwidth of 4 GHz. The target and the phase calibrator J1058+0133 were observed in ten-minute cycles, with eight minutes on the former and two minutes on the latter. The distance between the target and the phase calibrator was about 2.84° . Each observation included scans on the flux and bandpass calibrator J1331+3030 (3C286). The data were calibrated using the custom CASA pipeline (Version 6.5.4; McMullin et al. 2007) and visually inspected for possible radio frequency interference. The final images were produced with the `tclean` task in CASA (Version 5.5.0). A point-like source was detected at both frequencies at the position $\text{RA}(J2000) = 10:47:11.485$, $\text{Dec}(J2000) = +01:16:35.41$, with an uncertainty of $0.1''$. The final flux density error was estimated as the squared sum of the root mean square (RMS) and a typical 5% accuracy for the amplitude scale calibration. The results of the analysis are reported in Table 2.

In addition, we retrieved the results of the first VLA observations of GRB 240218A obtained on February 23 2024, beginning at 09:38:35 UT (5.32 days post-burst) and lasting 2.5 hours at multiple frequencies (Schroeder et al. 2024). A radio source at a mean frequency of 9.8 GHz with a flux density of $\sim 280 \mu\text{Jy}$ was found at the position: $\text{RA}(J2000) = 10:47:11.480$, $\text{Dec}(J2000) = +01:16:35.29$, with an uncertainty of $\sim 0.2''$ in each coordinate. This is consistent with the X-ray and NIR positions.

2.4.2. ATCA

Following the determination of the spectroscopic redshift, radio observations were obtained with the Australian Telescope Compact Array (ATCA) under programme C3546 (PI Thakur) for high-redshift GRB follow-up. Observations were obtained in the C and X bands at three epochs, 15, 33, and 48 days post-burst. The datasets were processed in Miriad (Sault et al. 1995) using standard flagging, calibration, and imaging procedures. The primary and bandpass calibrator was 1934-638 and the phase

calibrator was 1038+064. At the Fourier inversion stage, a robustness parameter of $r = 0$ was chosen to maximise the sensitivity of a detection experiment. The afterglow was detected at a location consistent with the X-ray and NIR positions. Flux densities were evaluated at the source peak position in the restored images, as this is the best estimate for point-like sources. The RMS noise in the final radio maps was computed away from the target and bright side sources. The multiplicative term related to residual gain calibration errors, evaluated to be 5% for 4-cm receivers, was negligible in the flux density error budget as the source was detected with low enough signal-to-noise. The results are reported in Table 2.

2.4.3. e-MERLIN

To improve the angular resolution and exclude possible confusing sources in the field of the GRB, we also requested a Director’s Discretionary Time (DDT) observations with the Enhanced Multi-Element Remotely Linked Interferometer Network (e-MERLIN, Project ID DD17002, PI Thakur). They were carried out in the C band and in two epochs, 15 and 18 days after the burst, including the following antennas: Mk2, Pi, Da, Kn, De, and Cm. The phase calibrator was 1048+0055, while 3C286 was adopted for amplitude calibration. Each run had a total duration of ~ 13 hours. Data were processed with the eMERLIN pipeline (eMCP; Moldon 2021), and imaging was performed with CASA (McMullin et al. 2007) at a central frequency of 5.1 GHz, adopting natural weighting. The source peak was derived from the image statistics, and RMS was measured in a region surrounding the target. The final flux density error was estimated as the squared sum of the RMS and a typical 10% accuracy for the amplitude scale calibration. We display the results for these observations in Table 2.

2.4.4. Other observations

The source was also detected with the Atacama Large Millimeter/Submillimeter Array (ALMA) in the millimetre band, at 97.5 GHz (Laskar et al. 2024). The observations began on March 2 2024 at 02:46:33 UT (13.0 d after the burst), and a millimetre source with a flux density of ~ 0.1 mJy was found at the position RA (J2000) = 10:47:11.5, Dec (J2000) = 1:16:36.0, with an uncertainty of $\sim 0.3''$ in each coordinate. This is consistent with the X-ray, NIR, and radio positions. Moreover, a 3σ upper limit of 65 μ Jy was obtained with NOEMA at 74 and 90 GHz at a mean epoch 10.88 days after the burst (de Ugarte Postigo et al. 2024).

3. Data analysis and results

3.1. Gamma-rays

We analysed the prompt emission spectrum by combining the *Fermi*/GBM and *Swift*/BAT data. The time-integrated spectrum of *Fermi*/GBM was accumulated over the time interval $[-2, 30]$ s (shaded yellow region in Fig. 2). The background spectrum was computed considering two time intervals before and after the one containing the burst. A third-order polynomial was fitted to these intervals and interpolated in the time interval of the burst. Data of NaI #1,2 and BGO1 were reduced with *Fermitools* 2.2.0. The spectrum corresponding to the peak time of the burst was extracted over the 1.024 s time interval shown by the cyan-shaded region in Fig. 2. We analysed *Swift*/BAT data and processed them with the standard *Swift* analysis software included

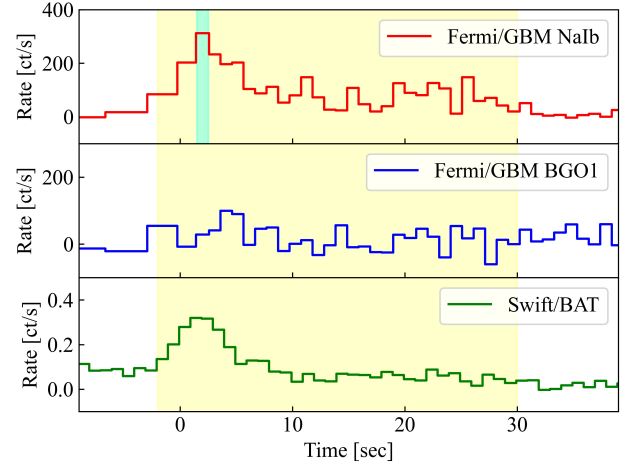


Fig. 2. *Fermi*/GBM and *Swift*/BAT (15–150 keV) light curve. The shaded yellow and cyan regions mark the time interval over which the time-integrated and peak spectra were extracted. The times were computed from the *Fermi*/GBM trigger time.

Table 1. Prompt emission spectral analysis results.

	$\log(L_{\text{iso}})$ [erg s $^{-1}$]	E_{break} [keV]	β_1	β_2	E_{peak} [keV]
$[-2, 30]$ s	$52.90^{+0.07}_{-0.09}$	$32.09^{+13.92}_{-8.22}$	$0.48^{+0.32}_{-0.64}$	$1.69^{+0.20}_{-0.19}$	293^{+343}_{-194}
Peak	$53.19^{+0.11}_{-0.11}$		$0.76^{+1.25}_{-0.80}$		134^{+47}_{-26}

Notes. Results of the spectral analysis of prompt emission *Swift*/BAT and *Fermi*/GBM data. β_1 and β_2 indicate the spectral slopes of the best-fit model (see Sect. 3.1).

in the NASA’s HEASARC software (HEASOFT, ver.6.31) and the relevant calibration files, and we extracted 15–150 keV BAT spectra and response matrices with the *batbinevt* tasks in FTOOLS in different time intervals. Since *Swift* was slewing after 10.5 s, we divided the time interval $[-2, 30]$ s into five sub-intervals, one pre-slew, $[-2, 10.5]$ s, and four during the slew, $[10.5, 30]$ s, each with a duration of 5 s so that the source is not appreciably moving in the BAT field of view.

The time-integrated spectrum of *Fermi*/GBM was fitted together with the five BAT spectra with the same model. We considered three spectral models with an increasing number of free parameters: a power law with a high energy cut-off (CPL), a smoothly broken power law (SBPL), and an SBPL with a high energy cut-off (SBPLCT). Both the SBPL and the SBPLCT produce a significantly better fit with respect to the CPL model and the best-fit parameters for the SBPLCT fit are reported in Table 1 along with their 95% confidence intervals. The posterior distributions of the model parameters are shown in Fig. B.1. The time-averaged spectrum is shown in Fig. 3. In Table 1, we also report the parameters of the fit of the peak spectrum, which, owing to the smaller signal, can only be fitted by a CPL model.

Adopting the results obtained, we then derived the burst rest-frame peak energy both from the time-integrated and the peak spectrum, yielding $E_{p,z} = 2280^{+2669}_{-1510}$ keV and $E_{p,z,\text{pk}} = 1043^{+366}_{-202}$ keV, respectively. The isotropic peak luminosity, L_{iso} , is reported in Table 1, while the isotropic equivalent energy is $\log(E_{\text{iso}}/\text{erg}) = 53.51^{+0.07}_{-0.09}$. We considered a complete, flux-limited sample of LGRBs, the BAT6 sample (Salvaterra et al. 2012), for a comparison with the population of long bursts. We found that GRB 240218A lies within

Table 2. GRB 240218A radio observations.

$t - t_0$ [d]	F_ν [μJy]	σ_{F_ν} [μJy]	Telescope	Frequency [GHz]
15	147	28	e-MERLIN	5.1
18	96.5	18.7	e-MERLIN	5.1
15	205	16	ATCA	5.5
33	<51	–	ATCA	5.5
48	<39	–	ATCA	5.5
8.13	131	16	VLA	6
18.19	115	10	VLA	6
38.08	<42	–	VLA	6
15	108	20	ATCA	9
33	39	10	ATCA	9
48	<30	–	ATCA	9
8.13	203	12	VLA	10
18.19	97	8	VLA	10
38.08	<24	–	VLA	10

Notes. Results for radio observations obtained with different facilities.

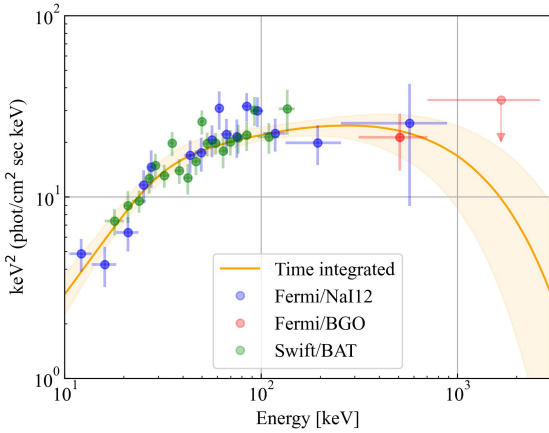


Fig. 3. Spectral energy distribution of the prompt emission spectrum, averaged over the $[-2, 30]$ s time interval. The SBPLCT model is shown by the solid line with the 68% confidence region shown by the shading. The data points are reported with their 1σ errors.

the 3σ confidence region (data from Nava et al. 2012) for the $E_{\text{iso}} - E_{p,z}$ Amati relation and the $L_{\text{iso}} - E_{p,z}$ Yonetoku relation. This tells us that GRB 240218A, like other high- z GRBs (Salvaterra 2015), is consistent with the population of LGRBs in terms of prompt-phase energetics.

3.2. X-rays

We retrieved the *Swift*/XRT light curve of GRB 240218A from the GRB XRT light curve repository³ (Evans et al. 2007, 2009). The light curve comprises 5.7 ks of data obtained from $t_0 + 137$ s to $t_0 + 149.4$ ks, 118 s of which are in windowed timing (WT) mode, and the remainder in photon counting (PC) mode. We fitted the light curve with a double-broken power law, excluding the WT-mode data from 188 s after the trigger, which are related to flaring activity in the X-rays. The best-fit yields the following results: the light curve initially decays with index $\alpha_1^X = -2.11 \pm 0.06$, then with $\alpha_2^X = -0.56 \pm 0.24$ from $t_0 + 1540$ s to $t_0 + 90259$ s, and at later times with $\alpha_3^X = -2.29 \pm 0.70$. The

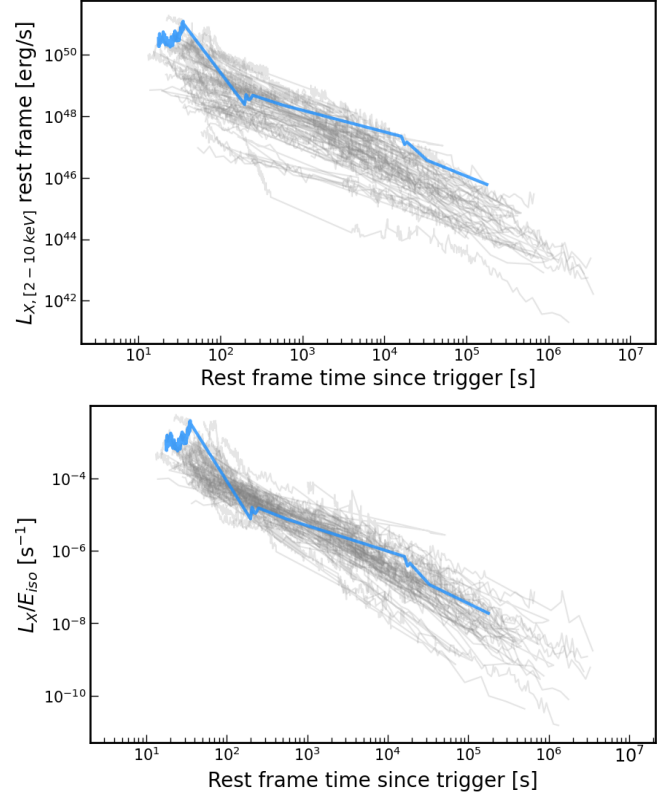


Fig. 4. *Top panel:* Rest frame X-ray light curve of GRB 240218A (blue line) compared with those of the BAT6 sample (grey curves), all in the common rest-frame energy range 2–10 keV. The burst is consistent with the most luminous curves of the sample. *Bottom panel:* Same as above but normalised with respect to the isotropic equivalent energy, E_{iso} (data for the BAT6 sample from Nava et al. 2012). GRB 240218A is fully consistent with the population of LGRBs.

$\chi^2/\text{d.o.f.}$ decreases from 1.40 to 1.26 with respect to a fit with a broken power law. The XRT spectral analysis is not discussed here, but we refer to Sect. 3.5 in the broader context of the SED analysis.

Besides the prompt phase correlations presented above, D’Avanzo et al. (2012) derived prompt-afterglow correlations for the BAT6 sample comparing the prompt phase quantities with the rest-frame X-ray luminosity at different rest-frame times: 5 min, 1 h, 11 h, and 24 h. We put the X-ray light curve in the burst rest frame to test its consistency with the LGRBs belonging to the BAT6 sample. We first retrieved the observed 0.3–10 keV unabsorbed fluxes and the time-resolved measured photon spectral index, Γ , from the *Swift* Burst Analyser⁴ (Evans et al. 2009), then we used the relation

$$f_X^{\text{rf}}(2-10 \text{ keV}) = f_X(0.3-10 \text{ keV}) \frac{\left(\frac{10}{1+z}\right)^{2-\Gamma} - \left(\frac{2}{1+z}\right)^{2-\Gamma}}{10^{2-\Gamma} - 0.3^{2-\Gamma}} \quad (1)$$

to obtain the light curve in the rest-frame 2–10 keV energy band. The luminosity was then obtained considering the luminosity distance of the burst. We show it and the curves of the BAT6 sample in the top panel of Fig. 4: the GRB 240218A light curve is fully consistent with the range spanned by BAT6 long GRBs; in particular, it lies on the region of the most luminous curves of the distribution, as is expected, it being a

³ https://www.swift.ac.uk/xrt_curves/01215912

⁴ http://www.swift.ac.uk/burst_analyser/

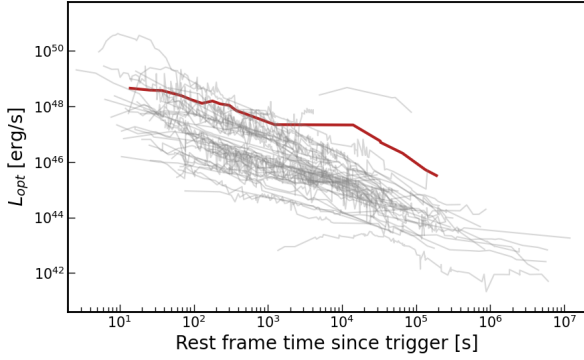


Fig. 5. Rest frame optical-NIR light curve of GRB 240218A (brown line) compared with those of the BAT6 sample (grey curves). The curves were corrected for Galactic and intrinsic absorption. GRB 240218A is consistent with the population of LGRBs at early times, while it is brighter by about one order of magnitude than all (but one) curves from $\sim 10^4$ s after the burst trigger.

high-redshift event. We also derived the X-ray rest frame light curve normalised to the E_{iso} for GRB 240218A and the BAT6 sample, and the curve is fully consistent with the population of LGRBs (see Fig. 4, bottom panel). This confirms the findings of Salvaterra (2015): high-redshift events do not show different E_{iso} -normalised X-ray rest-frame luminosity with respect to lower redshift bursts. We then obtained the X-ray luminosity at the four rest-frame times of 5 min, 1 h, 11 h, and 24 h from the best fit of the X-ray rest-frame light curve of GRB 240218A. These values were then compared with the prompt phase properties; that is, E_{iso} , L_{iso} , $E_{\text{p},z}$. Our results are consistent with the prompt-afterglow correlations derived by D’Avanzo et al. (2012), further strengthening the similarity of high- and low- z bursts in terms of X-ray luminosity compared to their rest-frame properties. We also re-analysed the CXO observation and we derived an unabsorbed flux in the 0.3–8 keV range of $F_{\text{X,CXO}} = 1.23^{+10.23}_{-0.91} \times 10^{-14} \text{ erg cm}^{-2} \text{ s}^{-1}$ (errors at 90% c.l.), consistent with that reported by Peña et al. (2024).

3.3. Optical, NIR, and radio

We analysed all the optical-NIR observations presented in Sect. 2.3 and we derived the afterglow magnitude by performing PSF photometry with the DAOPHOT (Stetson 1987) and ALLSTAR packages. All the NIR photometry was calibrated against the UKIDSS catalogue (Warren et al. 2007) using a common set of field stars. We present the results of the photometric analysis of the optical-NIR afterglow in Table A.1, and in Table 2 we summarise the radio flux densities from the observations described in Sect. 2.4. The H -band NIR curve was fitted with a double broken power law, obtaining a slope $\alpha_1^{\text{H}} = -0.63 \pm 0.10$ until $t_0 + 20417$ s, a flattening with decay $\alpha_2^{\text{H}} = 0.46 \pm 0.63$ up to $t - t_0 = 83176$ s, and a later time slope $\alpha_3^{\text{H}} = -1.63 \pm 0.14$. The decay of the last branch of the double broken power law in the X-ray and the NIR curves are consistent within a 1σ c.l., and the second break time in the NIR curve is close to that in the X-rays (see Sect. 3.2). These two results suggest a common origin for the emission.

Similar to the X-ray light curve, we put the observed NIR light curve in the rest frame by adopting the procedure applied by Melandri et al. (2014) for the curves of the BAT6 sample. We adopted the values derived from the analysis of the late-time SED (see Sect. 3.5) to put the observed data in the common U -

band rest frame and we show the results in Fig. 5. GRB 240218A light curve is fully consistent with LGRBs population at early time, then is brighter than the other curves but one. To investigate if this is a peculiar property of this event or is characteristic of high- z bursts we performed a deeper analysis of the event, as is presented in Sect. 3.6.

For the radio light curve, we modelled separately the data at 5.1, 5.5, and 6 GHz (C band) with a single power law from $t - t_0 = 1.3 \times 10^6$ s, with slope $\alpha^{\text{R}} = -2.86 \pm 0.57$, and the data at 9 and 10 GHz (X band) with a broken power law. For the X -band curve, we obtain a decay of $\alpha_1^{\text{R}} = -0.78 \pm 0.82$ before 1.19×10^6 s after the trigger and $\alpha_2^{\text{R}} = -1.34 \pm 0.36$ afterwards. The X -band, NIR, and X-ray late time decays are consistent with each other at the 1σ level, while the C -band slope is consistent at a 2σ c.l. The X-ray-to-radio light curves are shown in Fig. 6.

3.4. Combined analysis of X-ray and NIR light curves

We performed a combined X-ray-NIR light curve fit, covering a timescale from $\sim 10^2$ to $\sim 10^6$ s after the trigger, to investigate their evolution from early to late time. Radio data were thus excluded from this analysis since they were all obtained after $t - t_0 \sim 7 \times 10^5$ s. We used a single and double broken power law for the X-ray and NIR curves, respectively, with the X-ray break time and the second NIR break time fitted as a common parameter (t_b). Indeed, the late-time slopes obtained above may indicate that a jet break (Rhoads 1999) is present in the light curves. For the X-rays, only PC mode *Swift*/XRT data were considered for the fit since the WT mode data show high variability and flares. We fitted the data using maximum likelihood estimation and sampled the posterior distributions using the Python package emcee (Foreman-Mackey et al. 2013). We used uniform priors for each parameter listed in Table 3. The observations are in good agreement with the model, with the results for the fit reported in Table 3 and the contour plots shown in Fig. C.1. We note that $\alpha_{\text{X},1}/\alpha_{\text{H},1}$ and $\alpha_{\text{X},2}/\alpha_{\text{H},3}$ ratios are consistent at a 1σ level, in agreement with the results obtained from the analysis of the SED built at that time (see Sect. 3.5), which supports the jet break nature for the common break. The $\alpha_{\text{H},2}$ parameter, despite the considerable uncertainty stemming from the paucity of NIR data between 10^4 and 10^5 s after the burst, is consistent with a plateau. Moreover, the value we derived for the *Chandra* observation is consistent with the extrapolation of our fit.

To assess the goodness of the result, we also performed a fit with two separate parameters for the X-ray break time and the second NIR break time, yielding $\log(t_{\text{XRT}}/\text{s}) = 4.90^{+0.46}_{-0.47}$ and $\log(t_{\text{H}}/\text{s}) = 4.96^{+0.11}_{-0.20}$, respectively. They are consistent at a 1σ level with each other and with the common break parameter, t_b . Moreover, from a Bayesian information criterion (BIC; Schwarz 1978) test the model with the common break time is preferred, with $\Delta\text{BIC} \approx 4$. As a last check, we also performed a fit with a double broken power law model for both curves, and we found $\Delta\text{BIC} \approx 2.4$ with respect to the model presented above. Therefore, there is no strong evidence of a better fit of the X-ray curve with a double broken power law rather than with a single broken power law model.

3.5. SED modelling

We identified four time intervals (the grey-shaded areas in Fig. 6) to build SEDs including observations at different frequencies from the multi-wavelength data collected for GRB 240218A. The first time interval ($t \sim 150$ s after the trigger) includes data from *Swift*/BAT, *Swift*/XRT, and REM, from the gamma-rays to

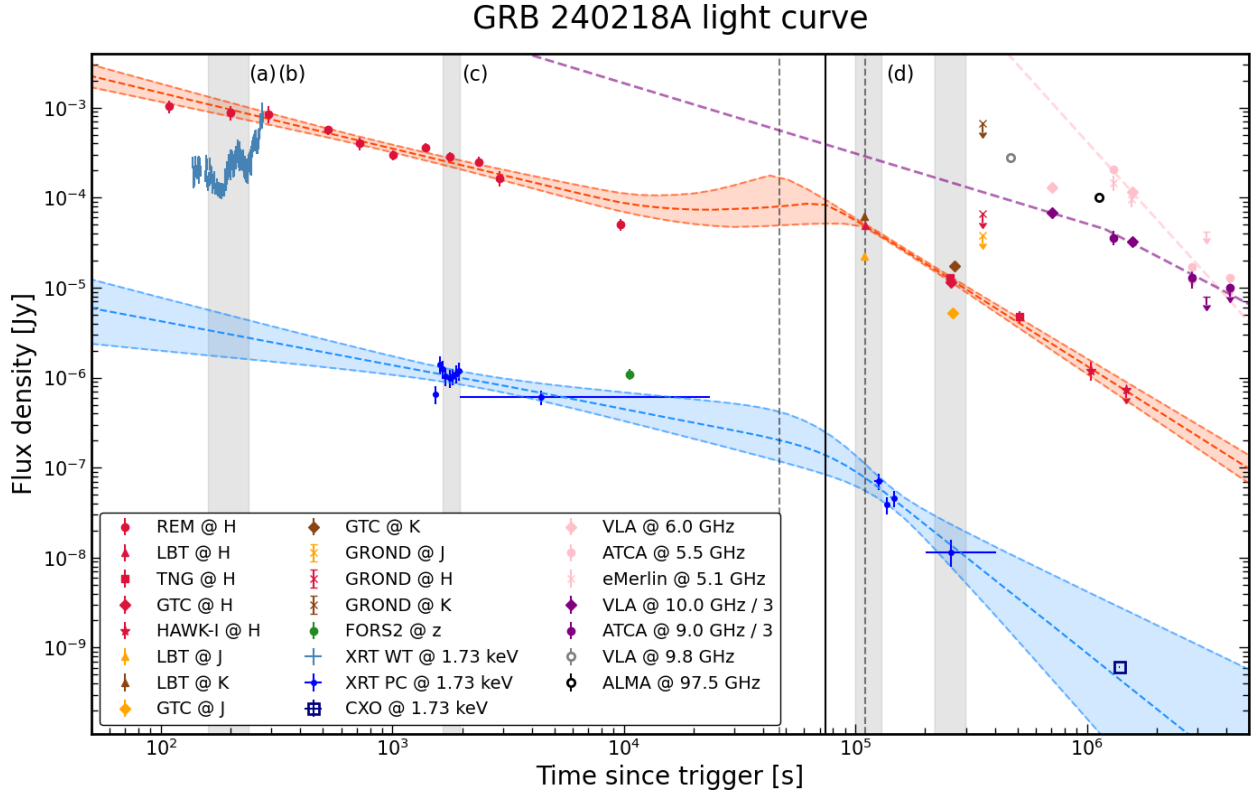


Fig. 6. X-rays and NIR light curves, along with the best fit and 1σ errors shown with dashed coloured lines. The vertical black lines mark the common break time (solid line) along with its errors (dashed lines). The X-ray light curve is computed at 1.73 keV, the log-mean of the XRT band. The radio light curves are also shown with their power-law best-fit results presented in Sect. 3.3, and empty points report data taken from GCNs. The vertical grey-shaded areas indicate the data used for SED modelling (see Sect. 3.5), and the letters next to them refer to the SEDs shown in Fig. 7. Optical upper limits are not shown for display purposes.

Table 3. X-ray/NIR light curve fit results.

Parameter	Value
$\alpha_{X,1}$	$-0.49^{+0.25}_{-0.18}$
$\alpha_{X,2}$	$-2.04^{+0.80}_{-0.88}$
$\alpha_{H,1}$	$-0.62^{+0.09}_{-0.09}$
$\alpha_{H,2}$	$0.41^{+0.88}_{-0.49}$
$\alpha_{H,3}$	$-1.63^{+0.10}_{-0.11}$
t_H [s]	$16\,218^{+20\,090}_{-6668}$
t_b [s]	$74\,132^{+25\,516}_{-27\,358}$

Notes. Results for the X-ray/NIR light curves best fit, with a common break time t_b in the two bands. t_H is the first break time in the NIR light curve. Reported values are the median of the posterior distributions; errors are at the 1σ level.

the H band. The second one ($t - t_0 \sim 10^3$ s) comprises observations from XRT and REM; the third ($t \sim 1.26$ d after the trigger) and fourth ($t - t_0 \sim 3$ d) from the X-rays to the K_S band from XRT-LBT and XRT-GTC, respectively.

Data analysis was carried out by modelling BAT, XRT, and NIR data together by the JSPEC package⁵ in a Bayesian framework. NIR extinction (UV in the rest-frame) was modelled following a Small-Magellanic Cloud recipe (Gordon et al. 2016) as

implemented in the Dust Extinction package⁶. Other recipes did not provide an acceptable fit to the data. X-ray extinction was modelled following Morrison & McCammon (1983) as implemented in the FittingFunction package⁷. The model was developed within the Turing probabilistic framework⁸.

In the early-time SED, the second NIR observation is simultaneous to the XRT-WT data, which show large flaring activity. Later, the observed X-ray flux drops by $\sim 2-3$ order of magnitudes, suggesting that the γ and X-ray emission at early time are produced in the prompt phase. With the aim of tracking a possible spectral evolution within this time interval, we split the NIR datapoint obtained with REM into five sub-intervals. Indeed, it is possible to obtain five sub-frames from each REM observation, as is explained in Sect. 2.3.1, and the afterglow flux can be derived for each. In principle, a BAT-to-REM SED can be derived for every sub-interval, but we obtained a detection with REM in the first two sub-frames only. For this reason, we modelled the SED from the gamma rays to the NIR in these two intervals. The $E(B - V)$ and the $\log(N_H)$ parameters were fixed due to the sparse statistics, leaving the other parameters free. The two fixed values are well constrained by the analysis of the late-time SED, which can be safely associated with a pure afterglow emission (see below), yielding $E(B - V) = 0.12$ mag and $\log(N_H/\text{cm}^{-2}) = 21.0$. Given the low statistics, we did not separate the Galactic and intrinsic components of N_H ; therefore,

⁶ <https://github.com/JuliaAstro/DustExtinction.jl>

⁷ <https://github.com/stefanocovino/FittingFunction.jl.git>

⁸ <https://turing.ml/>

⁵ <https://github.com/stefanocovino/JSPEC.jl.git>

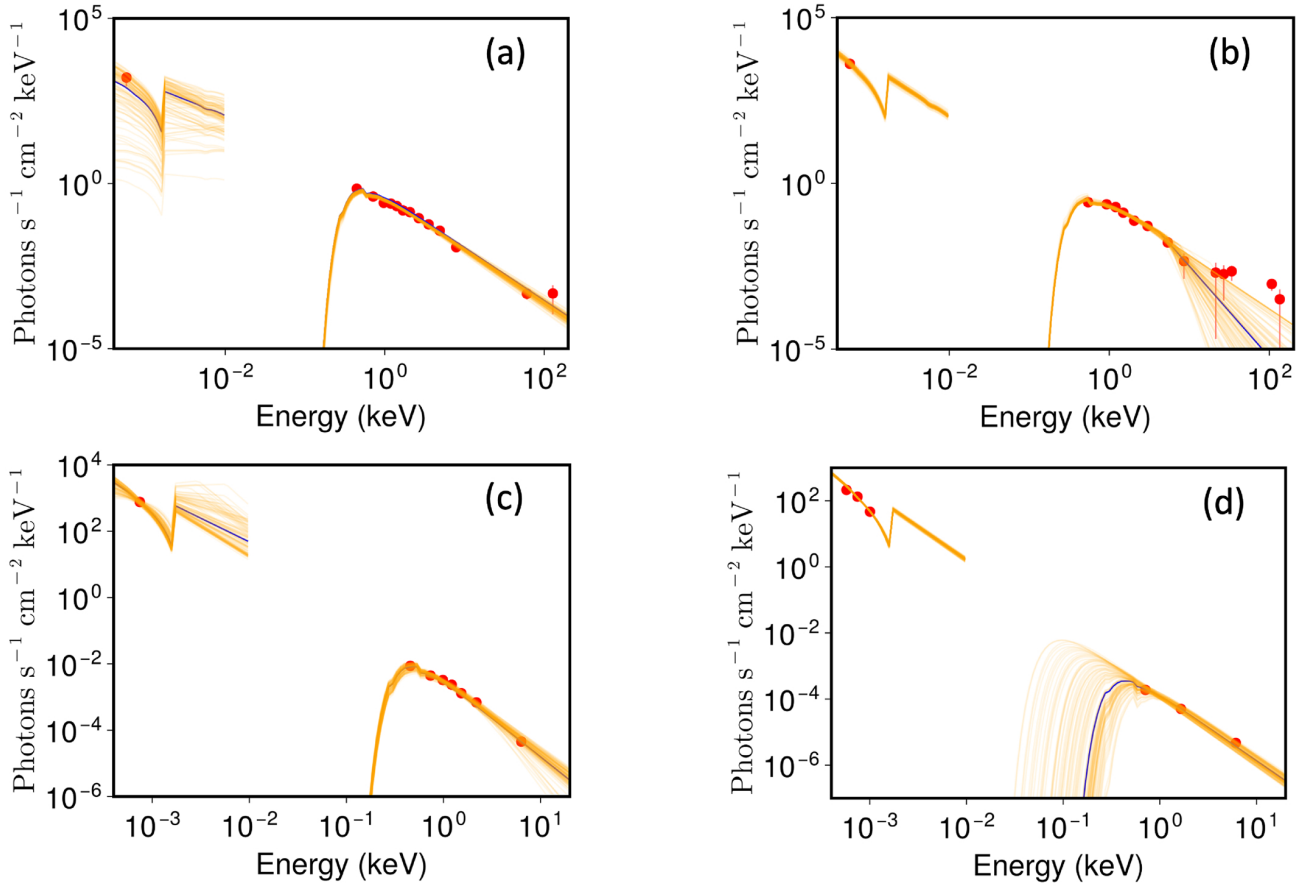


Fig. 7. Spectral energy distribution modelling of GRB 240218A at different times. The top figures refer to BAT, XRT, and REM data in the $t - t_0 = [160\text{--}170]$ s (left) and $[178\text{--}188]$ s (right) intervals (indicated by (a) and (b) in Fig. 6). The bottom left panel shows the SED including XRT and REM points taken $\sim 10^3$ seconds after the trigger, and the bottom right plot displays the modelling of XRT-LBT data at $t - t_0 = 1.26$ d. The best model for each SED (shown with blue lines in the plots) and the corresponding parameters are reported in Table 4.

Table 4. Spectral energy distribution modelling results.

Time interval (from t_0)	Data	Model	Parameters					p value
			Γ_1	Γ_2	E_b [keV]	$E(B - V)$ [mag]	$\log(N_H)$ [cm^{-2}]	
160–170 s	BAT + XRT + REM	SBPL	$-0.8^{+0.5}_{-0.3}$	$-1.6^{+0.05}_{-0.05}$	$0.06^{+0.19}_{-0.04}$	0.12^a	$21.0^{(a)}$	0.35
178–188 s	"	"	$-1.39^{+0.02}_{-0.02}$	$-2.9^{+0.9}_{-1.5}$	$4.27^{+1.48}_{-1.64}$	0.12^a	$21.0^{(a)}$	0.05
195–205 s	BAT + XRT	"	$-1.20^{+0.07}_{-0.07}$	$-1.82^{+0.15}_{-0.22}$	$7.76^{+4.26}_{-2.26}$	0.12^a	$21.0^{(a)}$	0.27
213–223 s	"	"	$-1.30^{+0.05}_{-0.06}$	$-2.8^{+0.5}_{-0.9}$	$7.04^{+2.09}_{-1.21}$	0.12^a	$21.0^{(a)}$	0.27
230–240 s	"	"	$-1.60^{+0.08}_{-0.07}$	$-2.6^{+0.6}_{-1.6}$	$10.0^{+29.8}_{-6.0}$	0.12^a	$21.0^{(a)}$	0.14
$\sim 10^3$ s	XRT + REM	SBPL	$-1.80^{+0.17}_{-0.04}$	$-2.4^{+0.5}_{-1.0}$	$1.6^{+1.5}_{-1.6}$	$0.12^{+0.01}_{-0.01}$	$20.6^{+0.6}_{-1.0}$	0.81
$\sim 10^3$ s	XRT + REM	SBPL	$-1.7^{+0.4}_{-0.1}$	$-2.4^{+0.1}_{-0.4}$	$0.20^{+1.06}_{-0.17}$	0.12^a	$21.0^{(a)}$	0.94
1.26–1.52 d	XRT + LBT (<i>JHK</i>)	PL	$-1.99^{+0.02}_{-0.03}$	–	–	$0.12^{+0.01}_{-0.01}$	$21.0^{+0.2}_{-0.4}$	0.05
2.98–3.06 d	XRT + GTC (<i>JHK</i>)	PL	$-1.99^{+0.02}_{-0.03}$	–	–	$0.12^{+0.01}_{-0.01}$	$21.0^{+0.3}_{-0.4}$	0.05

Notes. Spectral energy distribution analysis of GRB 240218A in different time intervals. The results coming from the best modelling are shown for each SED. The spectral slopes, Γ_1 and Γ_2 , are reported as photon indices ($\Gamma = \beta + 1$). The Bayesian p values shown in the last column were computed according to Lucy (2016, 2018). ^(a)Fixed parameter in the fit.

we modelled it at $z = 0$ also including the Galactic component $\log(N_{\text{H,Gal}}/\text{cm}^{-2}) = 20.6$ (Willingale et al. 2013). The model that best describes the early-time spectral behaviour is a SBPL. The top two panels of Fig. 7 show the results, and the best-fit values are presented in Table 4. For the three other sub-intervals without a NIR detection, we modelled the BAT-XRT SED and extrapolated the flux up to the *H* band to check if it was con-

sistent with the upper limit we obtained from the corresponding sub-frames. In all cases, the extrapolated NIR flux from the model is compatible with the limits derived from REM analysis, even if the large uncertainties yield a range of acceptable NIR fluxes spanning some orders of magnitude. From this analysis, it is not possible to safely state if the gamma, X-ray, and NIR emissions share the same physical origin. Unlike the high-energy

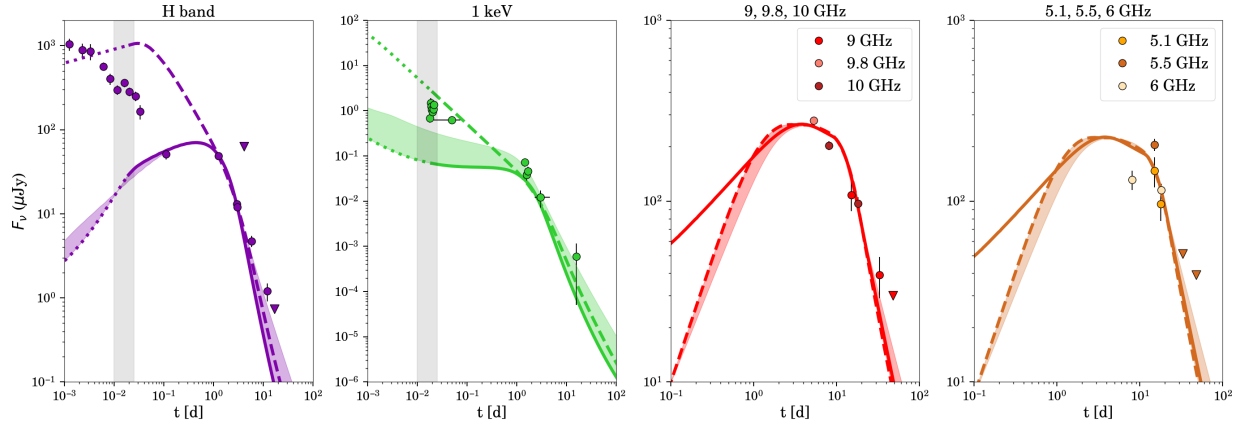


Fig. 8. Light curves in the optical, X-ray, and radio bands. The dashed lines show the on-axis top-hat model, while the solid lines represent the off-axis Gaussian model. The shaded coloured regions represent how the model changes with and without the spreading of the jet. In particular, the lower part of these regions represents the model with spreading (coinciding with the solid line), while the top part corresponds to the model without spreading. The vertical shaded regions in the first two panels represent the deceleration time 1σ region. Before that, a likely contribution from the late-time activity of the central engine is at play. Here, afterglow modelling is not reliable and data before 0.1 d from the trigger were excluded from the fit.

radiation, NIR data do not indicate flaring activity and the flux evolves with a shallow decay, so no drop is observed. Two main scenarios can be identified to explain the behaviour in the NIR band. First, the XRT variability is also present in the H band, but the additional contribution coming from the emerging afterglow makes this negligible and not observable. On the other hand, there can be no variability at NIR frequencies (e.g. Tanvir et al. 2009) and only a standard synchrotron emission powering the afterglow is at play. The presence of an additional contribution on top of the afterglow is suggested by the physical modelling described in Sect. 3.6.

We then modelled the SED in the second time interval at $t - t_0 \sim 10^3$ s, which includes XRT and REM observations. The model that best fits the data is again a SBPL. We performed the fit both with $E(B - V)$ and N_H values fixed from the late-time SED and leaving all the parameters free. The results from the two fits are consistent with each other and the optical extinction and the X-ray equivalent column density are compatible with the fixed value. We decided to keep the results with the two values fixed because of the better statistics and we show the fit in the bottom left panel of Fig. 7. Moreover, the break energy parameter is not very well constrained, but the addition of a spectral break between 0.01 and 10 keV yields a better fit compared to a simple power law model. The difference between the two spectral slopes is consistent with 0.5, which leads us to interpret this as the cooling break, assuming to be in the slow cooling regime (see e.g. Sari et al. 1998; Piran 2004).

The SED at $t - t_0 \sim 1.26$ d includes data from the X-rays to the K_S band, all obtained after the break time, t_b , found from the combined light curve fit. We modelled this SED with a simple power law (see Fig. 7, bottom right panel) with all parameters left free to vary. Indeed, the good statistics enabled us to constrain the optical extinction, $E(B - V)$, and the X-ray column density, N_H . Therefore, as was anticipated above, we adopted these values for the SED modelling when worse statistics prevented us from modelling the data with all parameters left free to vary. In addition, the derived value of Γ_1 is consistent with Γ_2 from the previous SED at $t - t_0 \sim 10^3$ s (see Table 4) and the cooling frequency dropped below the optical band at 1.26 d. These findings are consistent with expectations from the forward shock (FS) model in a uniform interstellar medium (ISM): the

spectral slopes do not vary, and the cooling break evolves as $\nu_c \propto t^{-1/2}$. Thus, our results suggest the presence of a homogeneous medium. The spectral slope obtained is also consistent with typical values expected for synchrotron emission from FS after t_b . This strengthens its interpretation as a jet break and confirms that the observed radiation at these times belongs to the afterglow phase. In the last SED, we considered XRT and GTC data taken at $t - t_0 \sim 3$ d, and the modelling yields the same results as the previous SED. For this reason, the corresponding plot is not shown. These analyses unambiguously confirm that the emission after t_b belongs to the afterglow phase and that the afterglow spectrum after the jet break does not evolve.

3.6. Broadband light curve physical modelling

Besides the empirical analyses of the X-ray/NIR light curves and of the SEDs reported above, we also included the radio data (all obtained after t_b) to fit the multi-band afterglow using the `afterglowpy` package (Ryan et al. 2020). It estimates the observer frame flux at a specific time and frequency depending on the input parameters. We performed two fits, assuming a top-hat and a Gaussian structure for the jet. The parameters describing the jet geometry are the jet core (half-)angle, θ_c , the jet total angular width, θ_w (only in the case of the Gaussian jet), the on-axis isotropic equivalent kinetic energy of the blast wave, E_0 , and the viewing angle (the angle between our line of sight and the jet axis), θ_v . The main part of the emission in the afterglow is from the FS-accelerated electrons that emit synchrotron radiation. Their energy distribution is a power law with slope $-p$, the fraction of their post-shock internal energy is ε_e , whereas the fraction of post-shock internal energy in the magnetic field is denoted by ε_B . The circumburst medium number density is n_0 . The luminosity distance and the redshift are fixed, and the fraction of electrons accelerated to the non-thermal energy distribution χ_N is fixed to 1.0. Moreover, we assumed a constant-density environment. We fitted the dataset using dynamic nested sampling (Python package `Dynesty`; Speagle 2020), using 1000 live points and multiple bounding ellipsoids as the bounding strategy. The priors are uniform for θ_w in $[0^\circ, 90^\circ]$, θ_c in $[0^\circ, 90^\circ]$, and p in $[2, 3]$; log-uniform for E_0 in $[50, 56]$, ε_e in $[-5, 0]$, ε_B in $[-5, 0]$, and n_0 in $[-3, 3]$; sinusoidal for θ_v in $[0^\circ, 90^\circ]$.

The fitted dataset is represented in Fig. 8, with four panels representing the H band, the X-rays and the radio bands. With the above modelling, a purely on-axis top-hat model (dashed line) fits the radio and X-ray light curves sufficiently well. However, it overpredicts the flux in the NIR before $t - t_0 \sim 1$ d. The corresponding corner plot is shown in Fig. D.1. The flat part of the optical light curve between 0.1 and 1 day is suggestive of an off-axis jet, indeed providing a good match to the data in the NIR, radio, and X-rays after ~ 0.1 d. The model underpredicts the early X-ray and NIR fluxes, which, in this context, could be due to some still-ongoing central engine activity, as is also supported by the observed flaring activity. This contrasts with the possible afterglow-only origin of the NIR emission at the early time mentioned in Sect. 3.5. Indeed, the deceleration time (estimated from the parameter results), at which the afterglow emission is expected to start, is represented by the vertical shaded grey region, which is superimposed on the early X-ray data points. Before that, afterglow modelling is not reliable; therefore, data before $t - t_0 < 0.1$ d were excluded from the fit. An alternative interpretation for the early-time observations could be the presence of a reverse shock (RS) component. Although a RS is typically linked to an optical flash (e.g. Yi et al. 2020), we do not observe such a clear signature in this case. However, our observations began at $t - t_0 = 68$ s, and the peak may have occurred earlier (see e.g. Vestrand et al. 2014). In this scenario, we are likely observing the decay phase following the flash, making it difficult to distinguish between this interpretation and the late-time activity of the central engine.

The off-axis Gaussian jet fit (corner plot is shown in Fig. E.1) suggests a very narrow jet with a significant kinetic energy (and a total jet energy of $\log(E_{\text{jet}}/\text{erg}) = 52.5$) and an ISM density of $\log(n/\text{cm}^{-3}) = 1.2$. These results include the spreading of the jet in the modelling and are represented by the lower boundary of the shaded regions shown in Fig. 8. In the non-spreading case (upper boundary of the shaded regions), the slope of the late-time light curve is shallower and fits the last data points in the optical band better. The parameters of this fit are very similar to the spreading case, and the corner plot is represented in Fig. E.2. In particular, we obtain a jet with a core opening angle of $\theta_c = 1.26^{+0.17}_{-0.06}$ deg, while the observer viewing angle is $\theta_v = 2.52^{+0.57}_{-0.29}$ deg. The off-axis Gaussian jet fit results, both in the case of a spreading and a non-spreading jet, are reported in Table 5. From our modelling, we cannot directly determine the initial Lorentz factor, Γ_0 . However, we can estimate its lower limit since it depends on the peak of the optical afterglow, under the assumption that the same jet powers both the prompt and the afterglow emission. Even if the optical peak is not identified in this case, it is located before the peak time due to the observer viewing angle, which is $t - t_0 \sim 0.5$ d. It is possible to estimate the initial Lorentz factor (Sari & Piran 1999) through the following equation:

$$\Gamma_0 \sim 270 \left(\frac{E_{\text{iso},53}}{n_1 \eta^3 t_{p,2}^3} \right)^{1/8}, \quad (2)$$

where $E_{\text{iso},53}$ is the isotropic equivalent energy in units of 10^{53} erg, n_1 is the circumburst density in units of 1 cm^{-3} , and $t_{p,2}$ is the time of the optical peak in units of 100 seconds. Adopting the modelling results, we derive a lower limit, $\Gamma_0 \gtrsim 80$, from which it is possible to compute the limit on the Doppler factor, $\delta \sim 14$. This allowed us to provide an estimate for the correction of E_{iso} and E_{peak} for the jet inclination (Amati 2006), taking into account the high-energy spectral index, β_2 , of the prompt emis-

Table 5. Broadband light curve physical modelling results.

Parameter	Spreading jet	Non-spreading jet
θ_v [rad]	$0.05^{+0.01}_{-0.01}$	$0.04^{+0.003}_{-0.005}$
θ_c [rad]	$0.01^{+0.002}_{-0.002}$	$0.01^{+0.001}_{-0.001}$
θ_w [rad]	$0.72^{+0.41}_{-0.44}$	$0.79^{+0.51}_{-0.46}$
$\log(E_0)$ [erg]	$54.72^{+0.11}_{-0.08}$	$55.10^{+0.08}_{-0.06}$
$\log(n_0)$ [cm^{-3}]	$1.24^{+0.35}_{-0.44}$	$1.79^{+0.23}_{-0.27}$
p	$2.05^{+0.01}_{-0.01}$	$2.11^{+0.02}_{-0.02}$
$\log(\varepsilon_e)$	$-0.13^{+0.11}_{-0.03}$	$-0.53^{+0.06}_{-0.07}$
$\log(\varepsilon_B)$	$-2.48^{+0.27}_{-0.21}$	$-4.70^{+0.19}_{-0.19}$

Notes. Results of the broadband light curve physical modelling with an off-axis Gaussian jet. The fit results for both a spreading and non-spreading jet are presented. The reported values represent the medians of the posterior distributions, with errors corresponding to the 16th and 84th percentiles. The corresponding corner plots are shown in Appendix E.

sion (see Table 1). We then obtain $E_{\text{iso,corr}} \gtrsim 2 \times 10^{54}$ erg and $E_{\text{p,z,corr}} \gtrsim 10^4$ keV. Thus, GRB 240218A is more energetic than the majority of LGRBs but still within the 3σ scatter region of the Amati relation, as we would expect given the small observer viewing angle, θ_v .

4. Discussion

The light curve of GRB 240218A was first empirically modelled with a series of power laws and requiring that the X-ray and NIR light curves share a common break, which we found to be at $t_b = t - t_0 \sim 74\,132 \text{ s} = 0.86 \text{ d}$. Here, we investigate its interpretation as a jet break by discussing the results further and comparing them with theoretical expectations. According to the standard external FS model for the afterglow emission, we expect a flux decrease, reflected in an achromatic steepening of the light curve, as the blast wave decelerates over the Lorentz factor $\Gamma_L \sim 1/\theta_{\text{jet}}$ (for $\Gamma_L \gg 1$; Mészáros & Rees 1999): this is known as jet break. This is first a geometrical effect: the observer has access to a larger portion of the jet, corresponding to $1/\Gamma_L$, as the jet expands and slows down, until its edges are reached at $\Gamma_L = 1/\theta_{\text{jet}}$, and the whole cone is observable (Rhoads 1999). This effect alone results in a post-jet break steepening as $t^{-3/4}$ or $t^{-1/2}$, in case of a uniform or wind-like ISM, respectively. One can also consider a lateral spreading of the jet, which leads to an exponential decay of its Lorentz factor and is reflected in a steeper post-jet break decay. From numerical simulations (e.g. van Eerten & MacFadyen 2012), it is not clear how significant the contribution of the sideways expansion is, even if it seems to provide a good estimate of the post-break decay index. The late-time indices in turn depend on the specific ordering of the self-absorption (ν_a), cooling (ν_c), and peak (ν_m) frequencies of the afterglow spectrum (Sari et al. 1999; Rhoads 1999). The most common case at typical jet break times is $\nu_a < \nu_m < \nu_c$, corresponding to a constant flux for $\nu < \nu_a$, to decays as $t^{-1/3}$ for $\nu_a < \nu < \nu_m$, and t^{-p} for $\nu > \nu_m$, where p is the index of the electron distribution, $n(e) \propto \gamma^{-p}$, and typically ranges from 2 to 3. This is valid for both a uniform and a wind-like ISM, and we considered the case $\nu > \nu_m$ for a comparison with our results. The late time slopes in the X-rays and H band are consistent with each other within 1σ errors and that of the NIR curve is significantly shallower than -2 , in contrast with expectations.

Generally, a possible explanation for this behaviour may be a prolonged activity of the central engine with an energy injection mechanism, which supplies additional energy to the ejecta and produces a less steep decay than expected. We computed the expected light curve decay after the jet break according to this hypothesis following the relations derived for a constant density medium and below the cooling frequency (Zhang et al. 2006; Panaitescu et al. 2006; de Pasquale et al. 2009; Racusin et al. 2009), yielding a slope of -1.58 . This result is consistent with the post-break decays obtained from our empirical model (see Sect. 3.4) both for the NIR and the X-ray curves within the uncertainties. A possible further qualitative argument supporting this interpretation may be the larger luminosity of the rest-frame NIR curve of GRB 240218A with respect to the LGRB population after $\sim 10^4$ seconds (see Fig. 5). However, the presence of a Gaussian jet without lateral expansion and observed slightly off-axis can explain the late-time behaviour, while the observations before $t - t_0 \sim 0.1$ days can be attributed to prolonged activity from the central engine, as is discussed in Sect. 3.6. Moreover, the broadband modelling of the afterglow with a Gaussian jet structure yields a jet break time consistent with that derived from our empirical broken-power law description, confirming what we estimated without a physical model and supporting the interpretation of t_b as the jet break.

To properly discuss the jet opening angle, θ_{jet} , of GRB 240218A compared to the GRBs population, we note that in most cases it can only be estimated assuming a top-hat jet, both for low- and high-redshift events. For this reason, we estimated θ_{jet} for GRB 240218A from the jet break time under this assumption. We used the formulae from Rhoads (1999), Sari et al. (1999), Frail et al. (2001) for a uniform ISM:

$$\theta_{\text{jet}} = 6.88 \left(\frac{t_b^3 n_1}{E_{K,53} (1+z)^3} \right)^{1/8} \text{ deg}, \quad (3)$$

where the break time, t_b , is expressed in days, n_1 is the circumburst density n in units of 1 cm^{-3} , and $E_{K,53}$ is the kinetic energy of the outflow assuming isotropy in units of 10^{53} erg. A typical value for the efficiency, $\eta = E_{\gamma,\text{iso}}/E_{\text{tot}} = 0.2$, were adopted for consistency with previous studies on high- z GRBs (e.g. Melandri et al. 2015; Rossi et al. 2022). We obtained $\theta_{\text{jet}} = 2.20^{+0.32}_{-0.39}$ deg, from which we then corrected the isotropic equivalent energy to $E_{\gamma} = E_{\gamma,\text{iso}}(1 - \cos \theta_{\text{jet}}) = 2.41^{+1.31}_{-1.08} \times 10^{50}$ erg. The jet opening angle we estimated is narrower than for the majority of long GRBs, for which the median value for bursts at $z \sim 1$ is $\theta_{z \sim 1} = 7.4^{+11}_{-6.6}$ deg (errors at a 90% c.l.; Laskar et al. 2014). For high- z GRBs, Laskar et al. (2014) analysed three events, namely GRBs 050904, 090423, and 120521C, and found a mean value of $\theta_{z > 6} \sim (3.6 \pm 0.7)$ deg, which is a bit larger than the one derived for GRB 240218A. Lower values for the jet opening angle are not unprecedented and they are consistent with the average value of the sample of LGRBs with an early ($t - t_0 \lesssim 1$ d) jet break, $\theta_{\text{jet}} = (2.5 \pm 1.0)$ deg (Wang et al. 2018). On the other hand, Rossi et al. (2022) derived $\theta_{\text{jet}} = (7.9 \pm 1.6)$ deg for GRB 210905A at $z = 6.312$, which would suggest a different behaviour, being more in agreement with the population of nearby events. In addition, Lloyd-Ronning et al. (2019, 2020a) investigated the dependence of the jet opening angle on the redshift and found that the θ_{jet} of high- z GRBs is, on average, narrower than that of closer events, as has also been suggested by Laskar et al. (2014, 2018). GRB 240218A supports the hypothesis of more collimated jets at high redshift since it agrees

with the $\theta_{\text{jet}} - (1+z)$ correlation derived by Lloyd-Ronning et al. (2020a). This correlation would imply a higher intrinsic rate of bursts at large distances, with important consequences for the properties of long GRB progenitors at high redshifts. First, narrower jets require denser stellar environments to facilitate their collimation and successful launching. Such higher stellar densities are expected if the IMF evolves with cosmic time, with a top-heavier mass function at larger z . Assuming that the stellar density scales with the progenitor mass and taking into account the anti-correlation between θ_{jet} and z it is possible to derive the expected dependence of the stellar density on the redshift. The result, as is shown by Lloyd-Ronning et al. (2020a), is consistent with proposed IMF evolution models (e.g. Davé 2008), and the necessary conditions for successful jet collimation and launching in terms of luminosity are met when assuming typical progenitor parameters and a relatively low radiative efficiency for some LGRBs (Lloyd-Ronning et al. 2020a). Progenitor properties are also closely tied to metallicity, with low-metallicity environments (more typical at high redshift) required to explain the observed narrow jet opening angles. Furthermore, if both the IMF and the θ_{jet} evolve with redshift the estimates of the SFR derived from the observed GRB rate must be revised including appropriate corrections (Lloyd-Ronning et al. 2020b). A potential alternative to explain the proposed correlation and the absence of large θ_{jet} for high- z GRBs involves selection biases. However, Lloyd-Ronning et al. (2020a) showed that the redshift distributions of GRBs with jet opening angle measurements and the overall GRB population are statistically equivalent, with the same relative fraction of θ_{jet} measurement ($\sim 1/3$) at both low and high redshift. This suggests that a significant fraction of GRBs with large opening angles at high- z is not missing from current samples. Indeed, even after accounting for strong truncation and selection effects, the anti-correlation remains statistically significant (Lloyd-Ronning et al. 2020a), despite being based on a dispersed sample with relatively few high- z GRBs. Despite these arguments, the different results derived for other bursts (e.g. GRB 210905A) would call for a larger sample of such events with determined jet break time to derive better constraints on this possible correlation. In addition, the future detection of high- z GRBs would allow us to test possible implications on the GRB rate at large redshift and the SFR across cosmic time. In the case of GRB 240218A, the core opening angle, θ_c , obtained from the Gaussian jet modelling (see Sect. 3.6) is lower than the values estimated here for a top-hat jet. Nevertheless, we can apply similar arguments as the discussion above: $\theta_c = 1.26^{+0.17}_{-0.06}$ deg is lower than the majority of the bursts, suggesting the possible presence of narrower jets at larger redshift, but is consistent (at 2σ level) with the average opening angle of LGRBs with early jet break derived by Wang et al. (2018).

Using the jet energy we derived coupled with the rest frame E_{peak} , we then investigated the $E_{\gamma} - E_{\text{peak}}$ relation (Ghirlanda relation; Ghirlanda et al. 2004). Considering the sample of LGRBs from Wang et al. (2018), GRB 240218A satisfies the Ghirlanda relation consistently with LGRBs with early jet break time. This, along with the consistency with the Amati and Yonetoku relations for LGRBs, further confirms that GRB 240218A is not different in terms of energetics from low redshift bursts, nor does it support the presence of different progenitors, such as Pop III stars, for high- z bursts. No indication of different properties for high-redshift GRBs can be drawn for the comparison of the jet energy with the beaming-corrected energy for other GRBs since this parameter spans a range as large as that for low- z events and no redshift evolution has been found

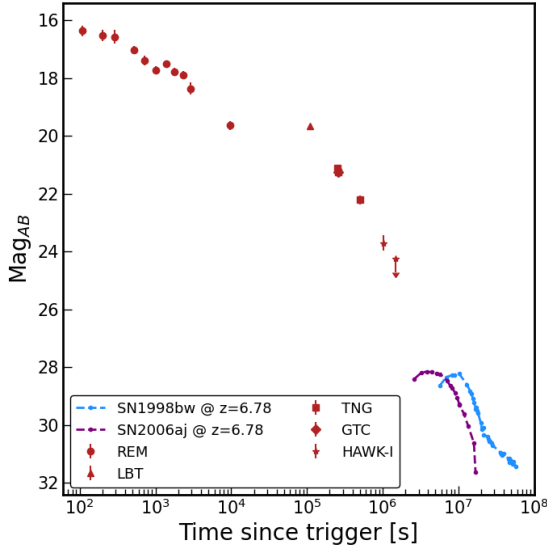


Fig. 9. Expected U -band equivalent rest-frame light curves for SN1998bw (blue line) and SN2006aj (purple line) at $z = 6.782$. They would peak at $t - t_0 = 118.5$ d and $t - t_0 = 44.2$ d, respectively.

(Lloyd-Ronning et al. 2019). The value we derive is similar to the median values for long GRBs, $\langle E_\gamma \rangle = 8.1^{+11}_{-4.3} \times 10^{50}$ erg (Laskar et al. 2014).

4.1. Supernova expectations at $z = 6.78$

A SN accompanying LGRBs is expected; therefore, we derived the magnitude that a typical GRB-related SN would reach at such a large distance. We collected the observed optical light curve of two paradigmatic SNe associated with LGRBs, namely SN1998bw (Galama et al. 1998) and SN2006aj (Campana et al. 2006), and put them at the distance corresponding to $z = 6.782$. In particular, we moved the U -band observed curves to the GRB rest frame, where the corresponding wavelength is $\sim 28\,000$ Å. This is within the $F277W$ filter of the *James Webb* Space Telescope (JWST), which is the only instrument to date with the capability to perform a follow-up at these distances (with an exposure of ~ 1 h), assuming that the SNe associated with a GRB at high redshift are similar to those observed so far related to lower z bursts. An SN1998bw-like SN would peak at $m_{AB} = 28.22$ after 118.5 days, while SN2006aj would reach the brightest magnitude of $m_{AB} = 28.15$ at $t - t_0 = 44.2$ d. The rest-frame light curves for the two SNe are shown in Fig. 9.

4.2. Dust extinction

The results obtained from the late-time SED analysis allow us to discuss the role of dust absorption for GRB 240218A and compare it with the population of LGRBs and other high- z GRBs in particular. Their host galaxies populate the faint end of the luminosity function (Salvaterra et al. 2011; Tanvir et al. 2012); therefore, low absorption is expected for such events, as was also found in previous studies on high-redshift bursts (see e.g. Zafar et al. 2010; Melandri et al. 2015; Zafar et al. 2018; Rossi et al. 2022). We obtained from our SED modelling $E(B - V) = 0.12$ mag, corresponding to $A_V = 0.35$ mag assuming an SMC-like extinction, and we compared it with the same values derived by Covino et al. (2013) for the LGRBs belonging to the BAT6 sample (see Fig. 10, top panel). Two populations were identified for the BAT6 LGRBs:

87% (50%) of the events display $A_V < 2$ ($A_V < 0.4$) mag while the remaining 13% are characterised by a large ($A_V > 2$ mag) extinction. The existence of a small population of highly extinguished bursts was also independently confirmed by Perley et al. (2016). We then retrieved the same quantities for high-redshift GRBs (see Melandri et al. 2015, their Table 5, and Rossi et al. 2022): their optical rest-frame extinction is consistent with GRB 240218A and with the LGRBs population showing negligible extinction. The absence of a population with large extinction at high- z is probably due to an observational bias since it is difficult to perform ground-based follow-up of locally high extinguished and distant events. These considerations could point to a redshift-independent behaviour of A_V .

We then computed the rest-frame X-ray hydrogen-equivalent column density $\log(N_{H,rf}/\text{cm}^{-2}) = 23.1$, which is consistent with the other high- z GRBs (Fig. 10, middle panel) and seems to confirm the possible redshift evolution for this parameter (see, e.g. Watson et al. 2013). As a consequence, also the N_H/A_V ratio indicates that higher values are obtained for most distant bursts (Fig. 10, bottom panel). However, this behaviour can be explained by the lack of low N_H values for high- z events because of absorption from intervening systems and the diffuse intergalactic medium along the line of sight (Campana et al. 2010, 2012; Starling et al. 2013). Indeed, the values derived for previous $z > 6$ GRBs and GRB 240218A are consistent with the effect of intervening material along the line of sight estimated by Campana et al. (2015). The effect would be thus independent of the progenitor and the local environment. Therefore, the results derived for GRB 240218A support the picture of $z > 6$ bursts displaying low optical extinction and large hydrogen-equivalent column density, with the latter ascribed to the effect of intervening systems along the line of sight.

5. Conclusions

GRB 240218A is a long GRB with the second-largest spectroscopically confirmed redshift, $z = 6.782$. We performed an extensive multi-wavelength follow-up of this event, from the gamma-rays to the radio, from 68 seconds after the burst was triggered by *Swift* up to ~ 48 days later. This allowed us to perform a complete analysis of this event, including the study of the light curve and the SED at different times.

The prompt phase observations obtained with *Swift*/BAT and *Fermi*/GBM allowed us to constrain the energetics of this event. It is fully consistent with lower redshift LGRBs from its compatibility with the Amati and Yonetoku relations. Moreover, from the X-ray observations, we found that it is consistent with the prompt-afterglow correlations derived for the population of LGRBs belonging to the BAT6 sample. Its rest-frame luminosity is large, yet not exceptional, and the E_{iso} -normalised rest-frame X-ray curve is consistent with the BAT6 sample.

The broadband (X-rays, NIR, and radio) light curve physical modelling from ~ 0.1 d is suggestive of the presence of a narrow, Gaussian jet observed slightly off-axis, leaving uncertain the origin of the early-time X-ray and NIR light curves. Both our empirical and physical models agree on the presence of a common break in the light curves at $t_b = 0.86$ d, which we interpret as the jet break. The SED analysis confirmed the afterglow origin for the late-time (i.e. after the jet break) observations, while the earlier emission interpretation is more complex: the X-ray emission is associated with the prompt phase, whereas the NIR emission probably comes from both the afterglow and additional contributions from a prolonged activity of the central engine or a RS. We also estimated the jet opening angle and the corre-

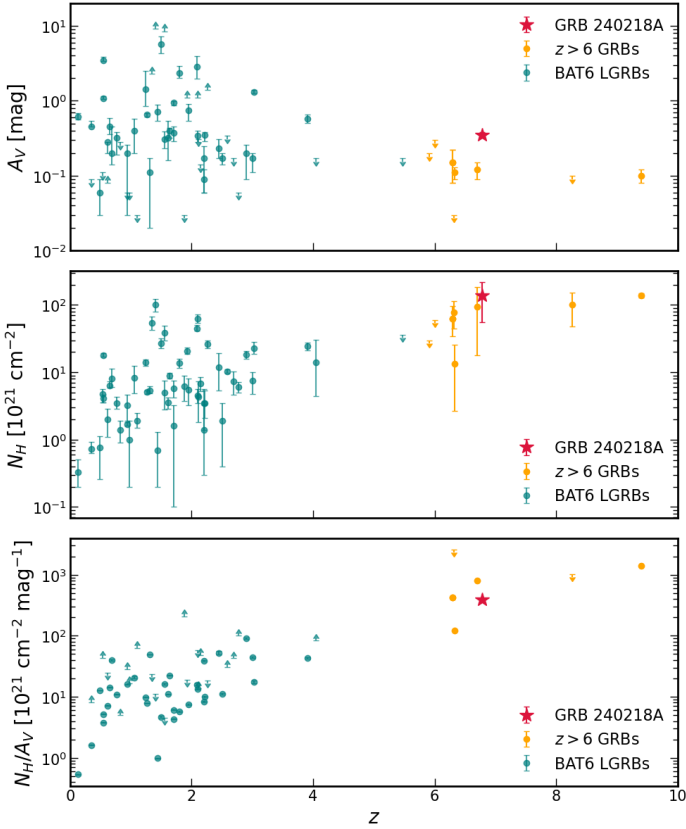


Fig. 10. Rest frame optical extinction (top panel) and X-ray hydrogen-equivalent column density (middle panel) of GRB 240218A compared with those of long GRBs belonging to the BAT6 sample and with other high- z GRBs. The ratio N_H/A_V is shown in the bottom panel, with only points for which at least one value between N_H and A_V is not a limit.

sponding beaming-corrected gamma-ray energy: the former is consistent with the interpretation of narrow opening angles for high- z events, as has already been suggested by Laskar et al. (2014) and Lloyd-Ronning et al. (2020a). However, this is not true for every high-redshift GRB (for example GRB 210905A; Rossi et al. 2022). Thus, only a larger sample of such events would help us better constrain this result.

The SED results also allowed us to compare the optical rest-frame extinction and the X-ray column density with those of the population of LGRBs and of other high- z bursts. GRB 240218A shows rest-frame A_V and N_H parameters that are fully consistent with high-redshift events. This confirms that the optical extinction of high- z GRBs is similar to the population of LGRBs with negligible A_V and a trend for the N_H with the redshift is present. However, the latter can be explained through the effect of intervening material along the line of sight, which also mimics the evolution of the N_H/A_V ratio with redshift.

This work confirms the importance of (promptly) following up on high-redshift GRBs to build a larger sample of such rare events. The combined effort of high-energy and lower-frequency facilities also allows us to acquire a broadband dataset that is crucial for properly interpreting and investigating these phenomena. New $z > 6$ GRBs are expected to be discovered by the recently launched *SVOM* (see Godet et al. 2014; Wei et al. 2016, for high- z GRB rate predictions) and Einstein Probe (Yuan et al. 2016) missions. Moreover, the foreseen launch of future missions, such as *THESEUS* (Amati et al. 2018; Tanvir et al. 2021) and the Gamow Explorer (White et al. 2021), will open a window onto the high- z Universe, providing more and more data on these

distant events. Comparable results can be obtained with HUGO (the High- z Universe GRB Observatory), shadowing from the ground the Rubin survey with a comparable field-of-view NIR telescope (Campana et al. 2022). This will also allow us to investigate some open questions, such as the evolution of the SFR and metallicity across cosmic time or the origin of Pop III stars.

Acknowledgements. Partly based on observations collected at the European Organisation for Astronomical Research in the Southern Hemisphere under ESO programme 110.24CF (PI Tanvir, Vergani, Malesani). This work made use of data supplied by the UK Swift Science Data Centre at the University of Leicester. The National Radio Astronomy Observatory is a facility of the National Science Foundation under cooperative agreement by Associated Universities, Inc. These observations were carried out as part of project SF161095, approved in the framework of the Fermi – NRAO joint program agreement. The LBT is an international collaboration of the University of Arizona, Italy (INAF: Istituto Nazionale di Astrofisica), Germany (LBTB: LBT Beteiligungsgesellschaft), the Ohio State University, representing also the University of Minnesota, the University of Virginia, and the University of Notre Dame. Partially based on observations made with the Gran Telescopio Canarias (GTC), installed at the Spanish Observatorio del Roque de los Muchachos of the Instituto de Astrofísica de Canarias, on the island of La Palma. S.Ca., P.D.A., M.F., M.G.B., T.S., and C.S. acknowledge funding from the Italian Space Agency, contract ASI/INAF n. I/004/11/6. A.R. acknowledges support by PRIN-MIUR 2017 (grant 20179ZF5KS). E.Mar. acknowledge support by INAF project Supporto Arizona & Italia. L.P., A.L.T. and G.Gi. acknowledge support by the European Union horizon 2020 programme under the AHEAD2020 project (grant agreement number 871158). L.P., A.L.T. and G.Gi. also acknowledge support by ASI (Italian Space Agency) through the Contract no. 2019-27-HH.0. The Australia Telescope Compact Array is part of the Australia Telescope National Facility (<https://ror.org/05qajvd42>) which is funded by the Australian Government for operation as a National Facility managed by CSIRO. We acknowledge the Gomeroi people as the Traditional Owners of the Observatory site. e-MERLIN is a National Facility operated by the University of Manchester at Jodrell Bank Observatory on behalf of STFC, part of UK Research and Innovation. R.R. acknowledges the support of the European Research Council through the Consolidator grant BHianca (Grant agreement ID: 101002761). G.B. acknowledges support from the European Union’s Horizon 2020 programme under the AHEAD2020 project (grant agreement no. 871158). DBM is supported by the European Union (ERC, HEAVYMETAL, 101071865). Views and opinions expressed are, however, those of the authors only and do not necessarily reflect those of the European Union or the European Research Council. Neither the European Union nor the granting authority can be held responsible for them. The Cosmic Dawn Center (DAWN) is funded by the Danish National Research Foundation under grant DNRF140. YDH thanks the financial support from INAF through the GRAWITA Large Program Grant (ID: 1.05.12.01.04). GT is grateful to the Programa de Apoyos para la Superación del Personal Académico, provided by the Dirección General de Asuntos del Personal Académico of UNAM, for invaluable support during my stay at the INAF, OAB, Italy. AJCT acknowledges support from the Spanish Ministry project PID2020-118491GB-I00 and PID2023-151905OB-I00 and Junta de Andalucía grant P20_010168 and from the Severo Ochoa grant CEX2021-001131-S funded by MCIN/AEI/ 10.13039/501100011033. AS acknowledges support from CNES and DIM-ACAV+.

References

- Amati, L. 2006, *MNRAS*, **372**, 233
 Amati, L., Frontera, F., Tavani, M., et al. 2002, *A&A*, **390**, 81
 Amati, L., O’Brien, P., Götz, D., et al. 2018, *Adv. Space Res.*, **62**, 191
 Appenzeller, I., Fricke, K., Fürstig, W., et al. 1998, *The Messenger*, **94**, 1
 Baffa, C., Comoretto, G., Gennari, S., et al. 2001, *A&A*, **378**, 722
 Band, D., Matteson, J., Ford, L., et al. 1993, *ApJ*, **413**, 281
 Barthelmy, S. D., Barbier, L. M., Cummings, J. R., et al. 2005, *Space Sci. Rev.*, **120**, 143
 Barthelmy, S. D., Krimm, H. A., Laha, S., et al. 2024, *GRB Coordinates Network*, **35761**, 1
 Bertin, E., & Arnouts, S. 1996, *A&AS*, **117**, 393
 Bertin, E., Mellier, Y., Radovich, M., et al. 2002, in *Astronomical Data Analysis Software and Systems XI*, eds. D. A. Bohlender, D. Durand, & T. H. Handley, *ASP Conf. Ser.*, **281**, 228
 Bloemen, S., Groot, P., Woudt, P., et al. 2016, in *Ground-based and Airborne Telescopes VI*, eds. H. J. Hall, R. Gilmozzi, & H. K. Marshall, *SPIE Conf. Ser.*, **9906**, 990664
 Bolmer, J., Greiner, J., Krühler, T., et al. 2018, *A&A*, **609**, A62

- Bromm, V., Yoshida, N., Hernquist, L., & McKee, C. F. 2009, *Nature*, **459**, 49
- Burrows, D. N., Hill, J. E., Nousek, J. A., et al. 2005, *Space Sci. Rev.*, **120**, 165
- Campana, S., Mangano, V., Blustin, A. J., et al. 2006, *Nature*, **442**, 1008
- Campana, S., Thöne, C. C., de Ugarte Postigo, A., et al. 2010, *MNRAS*, **402**, 2429
- Campana, S., Salvaterra, R., Melandri, A., et al. 2012, *MNRAS*, **421**, 1697
- Campana, S., Salvaterra, R., Ferrara, A., & Pallottini, A. 2015, *A&A*, **575**, A43
- Campana, S., Ghirlanda, G., Salvaterra, R., et al. 2022, *Nat. Astron.*, **6**, 1101
- Cano, Z., Wang, S.-Q., Dai, Z.-G., & Wu, X.-F. 2017, *Adv. Astron.*, **2017**, 8929054
- Chambers, K. C., Magnier, E. A., Metcalfe, N., et al. 2016, ArXiv e-prints [arXiv:1612.05560]
- Chornock, R., Berger, E., Fox, D. B., et al. 2013, *ApJ*, **774**, 26
- Corsi, A., & Lazzati, D. 2021, *New Astron. Rev.*, **92**, 101614
- Covino, S., Stefanon, M., Sciuto, G., et al. 2004, in *Ground-based Instrumentation for Astronomy*, eds. A. F. M. Moorwood, & M. Iye, *SPIE Conf. Ser.*, **5492**, 1613
- Covino, S., Melandri, A., Salvaterra, R., et al. 2013, *MNRAS*, **432**, 1231
- Cucchiara, A., Levan, A. J., Fox, D. B., et al. 2011, *ApJ*, **736**, 7
- D’Avanzo, P., Salvaterra, R., Sbaruffatti, B., et al. 2012, *MNRAS*, **425**, 506
- D’Avanzo, P., Ferro, M., Brivio, R., et al. 2024, *GRB Coordinates Network*, **35747**, 1
- Davé, R. 2008, *MNRAS*, **385**, 147
- de Pasquale, M., Evans, P., Oates, S., et al. 2009, *MNRAS*, **392**, 153
- de Ugarte Postigo, A., Laskar, T., Bremer, M., et al. 2024, *GRB Coordinates Network*, **35843**, 1
- Devillard, N. 1997, *The Messenger*, **87**, 19
- de Wet, S., Vreeswijk, P. M., & Groot, P. J. Meerlicht Consortium 2024, *GRB Coordinates Network*, **35765**, 1
- Evans, P. A., Beardmore, A. P., Page, K. L., et al. 2007, *A&A*, **469**, 379
- Evans, P. A., Beardmore, A. P., Page, K. L., et al. 2009, *MNRAS*, **397**, 1177
- Evans, P. A., Goad, M. R., Osborne, J. P., & Beardmore, A. P. Swift-XRT Team 2024, *GRB Coordinates Network*, **35748**, 1
- Foreman-Mackey, D., Hogg, D. W., Lang, D., & Goodman, J. 2013, *PASP*, **125**, 306
- Frail, D. A., Kulkarni, S. R., Sari, R., et al. 2001, *ApJ*, **562**, L55
- Freudling, W., Romaniello, M., Bramich, D. M., et al. 2013, *A&A*, **559**, A96
- Fruchter, A. S., Levan, A. J., Strolger, L., et al. 2006, *Nature*, **441**, 463
- Galama, T. J., Vreeswijk, P. M., van Paradijs, J., et al. 1998, *Nature*, **395**, 670
- Garzón, F., Balcells, M., Gallego, J., et al. 2022, *A&A*, **667**, A107
- Gehrels, N., Chincarini, G., Giommi, P., et al. 2004, *ApJ*, **611**, 1005
- Ghirlanda, G., Ghisellini, G., & Lazzati, D. 2004, *ApJ*, **616**, 331
- Godet, O., Nasser, G., Atteia, J., et al. 2014, in *Space Telescopes and Instrumentation 2014: Ultraviolet to Gamma Ray*, eds. T. Takahashi, J. W. A. den Herder, & M. Bautz, *SPIE Conf. Ser.*, **9144**, 914424
- Gordon, K. D., Fouesneau, M., Arab, H., et al. 2016, *ApJ*, **826**, 104
- Gou, L. J., Mészáros, P., Abel, T., & Zhang, B. 2004, *ApJ*, **604**, 508
- Greiner, J., Bornemann, W., Clemens, C., et al. 2008, *PASP*, **120**, 405
- Greiner, J., Krühler, T., Fynbo, J. P. U., et al. 2009, *ApJ*, **693**, 1610
- Grieco, V., Matteucci, F., Meynet, G., et al. 2012, *MNRAS*, **423**, 3049
- Hartoog, O. E., Malesani, D., Fynbo, J. P. U., et al. 2015, *A&A*, **580**, A139
- Hjorth, J., & Bloom, J. S. 2012, *Chapter 9 in “Gamma-Ray Bursts”*, 169
- Hjorth, J., Sollerman, J., Møller, P., et al. 2003, *Nature*, **423**, 847
- Jakobsson, P., Hjorth, J., Malesani, D., et al. 2012, *ApJ*, **752**, 62
- Kann, D. A., White, N. E., Ghirlanda, G., et al. 2024, *A&A*, **686**, A56
- Kawai, N., Kosugi, G., Aoki, K., et al. 2006, *Nature*, **440**, 184
- Kissler-Patig, M., Pirard, J. F., Casali, M., et al. 2008, *A&A*, **491**, 941
- Kistler, M. D., Yüksel, H., Beacom, J. F., & Stanek, K. Z. 2008, *ApJ*, **673**, L119
- Krühler, T., Küpcü Yoldaş, A., Greiner, J., et al. 2008, *ApJ*, **685**, 376
- Küpcü Yoldaş, A., Krühler, T., Greiner, J., et al. 2008, in *American Institute of Physics Conference Series*, eds. M. Galassi, D. Palmer, & E. Fenimore, **1000**, 227
- Laskar, T., Berger, E., Tanvir, N., et al. 2014, *ApJ*, **781**, 1
- Laskar, T., Berger, E., Chornock, R., et al. 2018, *ApJ*, **858**, 65
- Laskar, T., Peña, C., Schroeder, G., & Alexander, K. D. 2024, *GRB Coordinates Network*, **35878**, 1
- Leja, J., Speagle, J. S., Johnson, B. D., et al. 2020, *ApJ*, **893**, 111
- Lloyd-Ronning, N. M., Aykatalp, A., & Johnson, J. L. 2019, *MNRAS*, **488**, 5823
- Lloyd-Ronning, N., Hurtado, V. U., Aykatalp, A., Johnson, J., & Ceccobello, C. 2020a, *MNRAS*, **494**, 4371
- Lloyd-Ronning, N. M., Johnson, J. L., & Aykatalp, A. 2020b, *MNRAS*, **498**, 5041
- Lucy, L. B. 2016, *A&A*, **588**, A19
- Lucy, L. B. 2018, *A&A*, **618**, A100
- Malesani, D. B. 2024, *GRB Coordinates Network*, **35749**, 1
- Malesani, D. B., & Le Floch, E. Stargate Collaboration 2024, *GRB Coordinates Network*, **35743**, 1
- Matsumoto, T., Harikane, Y., Maeda, K., & Ioka, K. 2024, *ApJ*, **976**, L16
- McMullin, J. P., Waters, B., Schiebel, D., Young, W., & Golap, K. 2007, in *Astronomical Data Analysis Software and Systems XVI*, eds. R. A. Shaw, F. Hill, & D. J. Bell, *ASP Conf. Ser.*, **376**, 127
- Melandri, A., Covino, S., Rogantini, D., et al. 2014, *A&A*, **565**, A72
- Melandri, A., Bernardini, M. G., D’Avanzo, P., et al. 2015, *A&A*, **581**, A86
- Mészáros, P., & Rees, M. J. 1999, *MNRAS*, **306**, L39
- Mészáros, P., & Rees, M. J. 2010, *ApJ*, **715**, 967
- Moldon, J. 2021, *Astrophysics Source Code Library* [record ascl:2109.006]
- Molinari, E., Vergani, S. D., Malesani, D., et al. 2007, *A&A*, **469**, L13
- Morrison, R., & McCammon, D. 1983, *ApJ*, **270**, 119
- Nava, L., Salvaterra, R., Ghirlanda, G., et al. 2012, *MNRAS*, **421**, 1256
- Page, K. L., Parsotan, T. M., Siegel, M. H., & Neil Gehrels Swift Observatory Team 2024a, *GRB Coordinates Network*, **35742**, 1
- Page, K. L., Beardmore, A. P., Ferro, M., et al. 2024b, *GRB Coordinates Network*, **35757**, 1
- Panaiteescu, A., Mészáros, P., Burrows, D., et al. 2006, *MNRAS*, **369**, 2059
- Patel, M., Warren, S. J., Mortlock, D. J., & Fynbo, J. P. U. 2010, *A&A*, **512**, L3
- Peña, C., Laskar, T., Schroeder, G., & Alexander, K. D. 2024, *GRB Coordinates Network*, **35877**, 1
- Perley, D. A., Tanvir, N. R., Hjorth, J., et al. 2016, *ApJ*, **817**, 8
- Piran, T. 2004, *Rev. Mod. Phys.*, **76**, 1143
- Pirard, J.-F., Kissler-Patig, M., Moorwood, A., et al. 2004, in *Ground-based Instrumentation for Astronomy*, eds. A. F. M. Moorwood, & M. Iye, *SPIE Conf. Ser.*, **5492**, 1763
- Planck Collaboration XIII. 2016, *A&A*, **594**, A13
- Racusin, J. L., Liang, E. W., Burrows, D. N., et al. 2009, *ApJ*, **698**, 43
- Rhoads, J. E. 1999, *ApJ*, **525**, 737
- Robertson, B. E., & Ellis, R. S. 2012, *ApJ*, **744**, 95
- Rossi, A., Frederiks, D. D., Kann, D. A., et al. 2022, *A&A*, **665**, A125
- Rossi, A., Maiorano, E., Stratta, G., D’Avanzo, P., & CIBO Collaboration 2024, *GRB Coordinates Network*, **35762**, 1
- Ryan, G., van Eerten, H., Piro, L., & Troja, E. 2020, *ApJ*, **896**, 166
- Saccardi, A., Vergani, S. D., De Cia, A., et al. 2023, *A&A*, **671**, A84
- Saccardi, A., Malesani, D. B., Palmerio, J. T., et al. 2024, *GRB Coordinates Network*, **35756**, 1
- Salvaterra, R. 2015, *J. High Energy Astrophys.*, **7**, 35
- Salvaterra, R., Della Valle, M., Campana, S., et al. 2009, *Nature*, **461**, 1258
- Salvaterra, R., Ferrara, A., & Dayal, P. 2011, *MNRAS*, **414**, 847
- Salvaterra, R., Campana, S., Vergani, S. D., et al. 2012, *ApJ*, **749**, 68
- Sanyal, D., Langer, N., Szécsi, D., Yoon, S., & Grassiell, L. 2017, *A&A*, **597**, A71
- Sari, R., & Piran, T. 1999, *A&AS*, **138**, 537
- Sari, R., Piran, T., & Narayan, R. 1998, *ApJ*, **497**, L17
- Sari, R., Piran, T., & Halpern, J. P. 1999, *ApJ*, **519**, L17
- Sault, R. J., Teuben, P. J., & Wright, M. C. H. 1995, in *Astronomical Data Analysis Software and Systems IV*, eds. R. A. Shaw, H. E. Payne, & J. J. E. Hayes, *ASP Conf. Ser.*, **77**, 433
- Schlaflly, E. F., & Finkbeiner, D. P. 2011, *ApJ*, **737**, 103
- Schroeder, G., Peña, C., Laskar, T., & Alexander, K. D. 2024, *GRB Coordinates Network*, **35794**, 1
- Schwarz, G. 1978, *Ann. Stat.*, **6**, 461
- Seifert, W., Appenzeller, I., Baumeister, H., et al. 2003, in *Instrument Design and Performance for Optical/Infrared Ground-based Telescopes*, eds. M. Iye, & A. F. M. Moorwood, *SPIE Conf. Ser.*, **4841**, 962
- Skrutskie, M. F., Cutri, R. M., Stiening, R., et al. 2006, *AJ*, **131**, 1163
- Speagle, J. S. 2020, *MNRAS*, **493**, 3132
- Starling, R. L. C., Willingale, R., Tanvir, N. R., et al. 2013, *MNRAS*, **431**, 3159
- Stetson, P. B. 1987, *PASP*, **99**, 191
- Suwa, Y., & Ioka, K. 2011, *ApJ*, **726**, 107
- Svinkin, D., Frederiks, D., Lysenko, A., et al. 2024, *GRB Coordinates Network*, **35758**, 1
- Tagliaferri, G., Antonelli, L. A., Chincarini, G., et al. 2005, *A&A*, **443**, L1
- Tanvir, N. R., Fox, D. B., Levan, A. J., et al. 2009, *Nature*, **461**, 1254
- Tanvir, N. R., Levan, A. J., Fruchter, A. S., et al. 2012, *ApJ*, **754**, 46
- Tanvir, N. R., Laskar, T., Levan, A. J., et al. 2018, *ApJ*, **865**, 107
- Tanvir, N. R., Le Floch, E., Christensen, L., et al. 2021, *Exp. Astron.*, **52**, 219
- Tody, D. 1986, in *Instrumentation in astronomy VI*, ed. D. L. Crawford, *SPIE Conf. Ser.*, **627**, 733
- Toma, K., Yoon, S.-C., & Bromm, V. 2016, *Space Sci. Rev.*, **202**, 159
- Toma, K., P. G., & van der Marel, R. P. 2007, *ApJ*, **655**, 30
- van Eerten, H. J., & MacFadyen, A. I. 2012, *ApJ*, **751**, 155
- Veres, P., Meehan, C., & Fermi Gamma-ray Burst Monitor Team 2024, *GRB Coordinates Network*, **35755**, 1
- Vernet, J., Dekker, H., D’Odorico, S., et al. 2011, *A&A*, **536**, A105
- Vestrand, W. T., Wren, J. A., Panaiteescu, A., et al. 2014, *Science*, **343**, 38
- Wang, X.-G., Zhang, B., Liang, E.-W., et al. 2018, *ApJ*, **859**, 160
- Warren, S. J., Cross, N. J. G., Dye, S., et al. 2007, ArXiv e-prints [arXiv:astro-ph/0703037]

- Watson, D., Zafar, T., Andersen, A. C., et al. 2013, *ApJ*, **768**, 23
- Wei, J., Cordier, B., Antier, S., et al. 2016, ArXiv e-prints [arXiv:1610.06892]
- White, N. E., Bauer, F. E., Baumgartner, W., et al. 2021, in *UV, X-Ray, and Gamma-Ray Space Instrumentation for Astronomy XXII*, ed. O. H. Sigmund, *SPIE Conf. Ser.*, **11821**, 1182109
- Willingale, R., Starling, R. L. C., Beardmore, A. P., Tanvir, N. R., & O'Brien, P. T. 2013, *MNRAS*, **431**, 394
- Woosley, S. E., & Bloom, J. S. 2006, *ARA&A*, **44**, 507
- Woosley, S. E., & Heger, A. 2006, *ApJ*, **637**, 914
- Yi, S.-X., Wu, X.-F., Zou, Y.-C., & Dai, Z.-G. 2020, *ApJ*, **895**, 94
- Yonetoku, D., Murakami, T., Nakamura, T., et al. 2004, *ApJ*, **609**, 935
- Yuan, W., Osborne, J. P., Zhang, C., & Willingale, R. 2016, *Chin. J. Space Sci.*, **36**, 117
- Zafar, T., Watson, D. J., Malesani, D., et al. 2010, *A&A*, **515**, A94
- Zafar, T., Möller, P., Watson, D., et al. 2018, *MNRAS*, **480**, 108
- Zerbi, R. M., Chincarini, G., Ghisellini, G., et al. 2001, *Astron. Nachr.*, **322**, 275
- Zhang, B., Fan, Y. Z., Dyks, J., et al. 2006, *ApJ*, **642**, 354
- ¹³ Space Science Data Center (SSDC) – Agenzia Spaziale Italiana (ASI), 00133 Roma, Italy
- ¹⁴ University of Messina, Mathematics, Informatics, Physics and Earth Science Department, Via F.S. D'Alcontres 31, Polo Papardo 98166, Messina, Italy
- ¹⁵ Observatoire de la Côte d'Azur, Université Côte d'Azur, Boulevard de l'Observatoire, 06304 Nice, France
- ¹⁶ Aix Marseille Univ., CNRS, LAM, Marseille, France
- ¹⁷ University of Cape Town Astronomy Department, Private Bag X3, Rondebosch 7701, South Africa
- ¹⁸ Clemson University, Department of Physics and Astronomy, Clemson, SC 29634-0978, USA
- ¹⁹ Thüringer Landessternwarte Tautenburg, Sternwarte 5, 07778 Tautenburg, Germany
- ²⁰ Astrophysics Research Institute, Liverpool John Moores University, Liverpool Science Park IC2, 146 Brownlow Hill, Liverpool L3 5RF, UK
- ²¹ Cosmic Dawn Center (DAWN), Copenhagen, Denmark
- ²² Niels Bohr Institute, University of Copenhagen, Jagtvej 128, 2200 Copenhagen N, Denmark
- ²³ Department of Astrophysics/IMAPP, Radboud University, 6525 AJ Nijmegen, The Netherlands
- ²⁴ School of Physics and Centre for Space Research, University College Dublin, Belfield D04 V1W8, Dublin, Ireland
- ²⁵ Aryabhata Research Institute of Observational Sciences (ARIES), Manora Peak, Nainital 263002, India
- ²⁶ Astronomical Institute Anton Pannekoek, University of Amsterdam, 1090 GE Amsterdam, The Netherlands
- ²⁷ Max-Planck-Institut für Extraterrestrische Physik, Giessenbachstraße 1, 85748 Garching, Germany
- ²⁸ INAF – Istituto di Radioastronomia, Via Gobetti 101, 40129 Bologna, Italy
- ²⁹ Dipartimento di Fisica, Università degli Studi di Roma 'Tor Vergata', Via della Ricerca Scientifica 1, 00133 Roma, Italy
- ³⁰ GEPI, Observatoire de Paris, Université PSL, CNRS, 5 place Jules Janssen, 92190 Meudon, France
- ³¹ School of Physics and Astronomy, University of Leicester, University Road, Leicester LE1 7RH, UK
- ³² Astronomical Institute, Czech Academy of Sciences, Fričova 298, Ondřejov, Czech Republic
- ³³ School of Mathematical and Physical Sciences, Macquarie University, NSW 2109, Australia
-
- ¹ INAF – Osservatorio Astronomico di Brera, Via E. Bianchi 46, 23807 Merate, (LC), Italy
- ² Università degli Studi dell'Insubria, Dipartimento di Scienza e Alta Tecnologia, Via Valleggio 11, 22100 Como, Italy
- ³ Como Lake centre for AstroPhysics (CLAP), DiSAT, Università dell'Insubria, Via Valleggio 11, 22100 Como, Italy
- ⁴ INAF – Istituto di Astrofisica e Planetologia Spaziali, Via Fosso del Cavaliere 100, 00133 Roma, Italy
- ⁵ Guangxi Key Laboratory for Relativistic Astrophysics, School of Physical Science and Technology, Guangxi University, Nanning 530004, China
- ⁶ INAF – Osservatorio Astronomico di Roma, Via Frascati 33, 00078 Monte Porzio Catone, (RM), Italy
- ⁷ INAF – Osservatorio di Astrofisica e Scienza dello Spazio, Via Piero Gobetti 93/3, 40129 Bologna, Italy
- ⁸ INAF – IASF Milano, Via Alfonso Corti 12, 20133 Milano, Italy
- ⁹ Universidad Nacional Autónoma de México, Instituto de Astronomía, Aptdo Postal 106, Ensenada 22860, Baja California, Mexico
- ¹⁰ Centro Astronómico Hispano en Andalucía, Observatorio de Calar Alto, Sierra de los Filabres, Gérgal, Almería 04550, Spain
- ¹¹ Instituto de Astrofísica de Andalucía (IAA-CSIC), Glorieta de la Astronomía s/n, 18008, Granada, Spain
- ¹² Ingeniería de Sistemas y Automática, Universidad de Málaga, Unidad Asociada al CSIC por el IAA, Escuela de Ingenierías Industriales, Arquitecto Francisco Peñalosa, 6, Campanillas, 29071 Málaga, Spain

Appendix A: Optical-NIR photometric data

In this appendix we provide the optical and NIR photometric dataset collected for GRB 240218A.

Table A.1. GRB 240218A optical-NIR photometry.

$t - t_0$ [s]	Mag (AB)	σ_{mag}	F_v [mJy]	σ_{F_v} [mJy]	Telescope	Instrument	Filter
108	16.36	0.18	1.040	0.172	REM	REMIR	<i>H</i>
200	16.53	0.20	0.887	0.163	REM	REMIR	<i>H</i>
292	16.57	0.24	0.855	0.189	REM	REMIR	<i>H</i>
526	17.02	0.12	0.565	0.062	REM	REMIR	<i>H</i>
718	17.39	0.17	0.402	0.063	REM	REMIR	<i>H</i>
1006	17.72	0.14	0.297	0.038	REM	REMIR	<i>H</i>
1390	17.51	0.12	0.360	0.040	REM	REMIR	<i>H</i>
1775	17.77	0.13	0.283	0.034	REM	REMIR	<i>H</i>
2351	17.90	0.14	0.251	0.032	REM	REMIR	<i>H</i>
2900	18.36	0.21	0.164	0.032	REM	REMIR	<i>H</i>
9623	19.64	0.16	0.051	0.007	REM	REMIR	<i>H</i>
109200	19.67	0.02	0.049	0.91×10^{-3}	LBT	LUCI	<i>H</i>
255947	21.12	0.05	0.013	0.60×10^{-3}	TNG	NICS	<i>H</i>
258054	21.24	0.05	0.012	0.53×10^{-3}	GTC	EMIR	<i>H</i>
355800	> 19.3	–	< 0.063	–	MPG	GROND	<i>H</i>
509760	22.19	0.16	4.74×10^{-3}	0.70×10^{-3}	TNG	NICS	<i>H</i>
1037460	23.70	0.26	1.20×10^{-3}	0.29×10^{-3}	VLT	HAWK-I	<i>H</i>
1468301	> 24.23	–	< 0.74×10^{-3}	–	VLT	HAWK-I	<i>H</i>
108960	20.51	0.02	0.023	0.42×10^{-3}	LBT	LUCI	<i>J</i>
355800	> 19.9	–	< 0.036	–	MPG	GROND	<i>J</i>
263373	22.11	0.09	5.20×10^{-3}	0.43×10^{-3}	GTC	EMIR	<i>J</i>
108780	19.42	0.07	0.062	0.004	LBT	LUCI	K_S
355800	> 16.8	–	< 0.631	–	MPG	GROND	K_S
266685	20.81	0.04	0.017	0.63×10^{-3}	GTC	EMIR	K_S
2160	> 20.33	–	< 0.027	–	MeerLICHT	WFC	<i>u</i>
1748	> 18.52	–	< 0.142	–	REM	ROS2	<i>g</i>
2160	> 21.61	–	< 8.24×10^{-3}	–	MeerLICHT	WFC	<i>g</i>
4051	> 22.30	–	< 4.37×10^{-3}	–	VLT	X-shooter	<i>g</i>
9403	> 20.56	–	< 0.022	–	REM	ROS2	<i>g</i>
1748	> 18.82	–	< 0.108	–	REM	ROS2	<i>r</i>
2160	> 21.21	–	< 0.012	–	MeerLICHT	WFC	<i>r</i>
3592	> 23.00	–	< 2.29×10^{-3}	–	VLT	X-shooter	<i>r</i>
9403	> 20.27	–	< 0.027	–	REM	ROS2	<i>r</i>
93617	> 25.20	–	< 3.02×10^{-4}	–	GTC	OSIRIS	<i>r</i>
94373	> 26.30	–	< 1.10×10^{-4}	–	VLT	FORS2	<i>r</i>
1748	> 18.20	–	< 0.191	–	REM	ROS2	<i>i</i>
2160	> 20.54	–	< 0.022	–	MeerLICHT	WFC	<i>i</i>
9403	> 19.51	–	< 0.057	–	REM	ROS2	<i>i</i>
90869	> 24.05	–	< 8.71×10^{-4}	–	GTC	OSIRIS	<i>i</i>
1748	> 17.79	–	< 0.278	–	REM	ROS2	<i>z</i>
2160	> 19.54	–	< 0.055	–	MeerLICHT	WFC	<i>z</i>
3750	> 21.50	–	< 9.12×10^{-3}	–	VLT	X-shooter	<i>z</i>
9403	> 18.44	–	< 0.153	–	REM	ROS2	<i>z</i>
10530	23.80	0.11	1.10×10^{-3}	0.11×10^{-3}	VLT	FORS2	<i>z</i>
93419	> 23.20	–	< 1.91×10^{-3}	–	GTC	OSIRIS	<i>z</i>

Notes. Results for the optical and NIR observations of GRB 240218A. Values without errors are upper limits at the 3σ c.l. The values are not corrected for Galactic extinction along the line of sight, $E(B - V) = 0.04$ mag (Schlafly & Finkbeiner 2011).

Appendix B: Contour plot for prompt-phase time-integrated spectrum

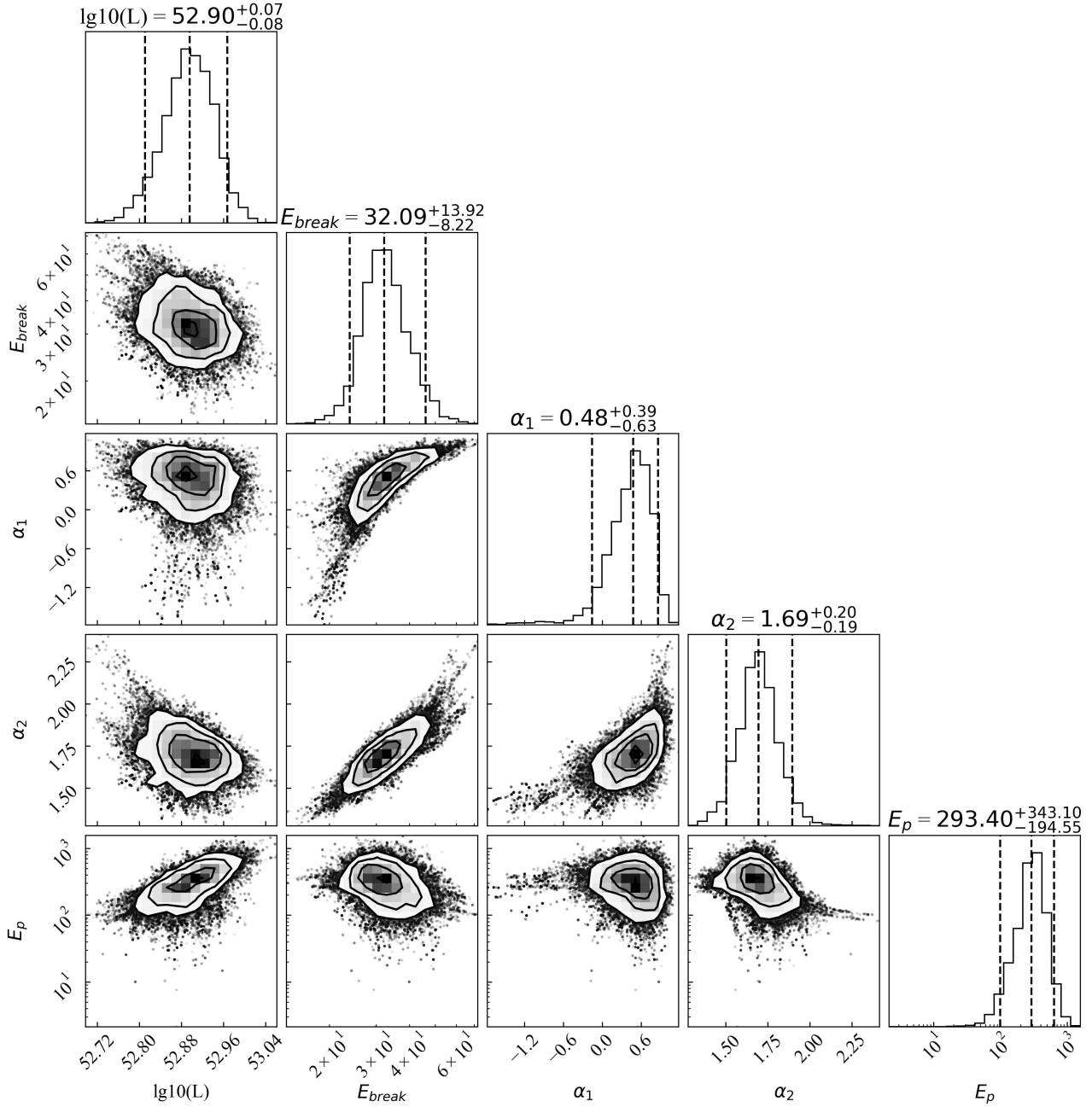


Fig. B.1. Posterior distribution of the model parameters for the fit of the time-integrated spectrum. Errors on the parameter values are 95% confidence intervals, E_{break} and E_p parameters are reported in units of keV.

Appendix C: Contour plot for X-ray/NIR light curve fit

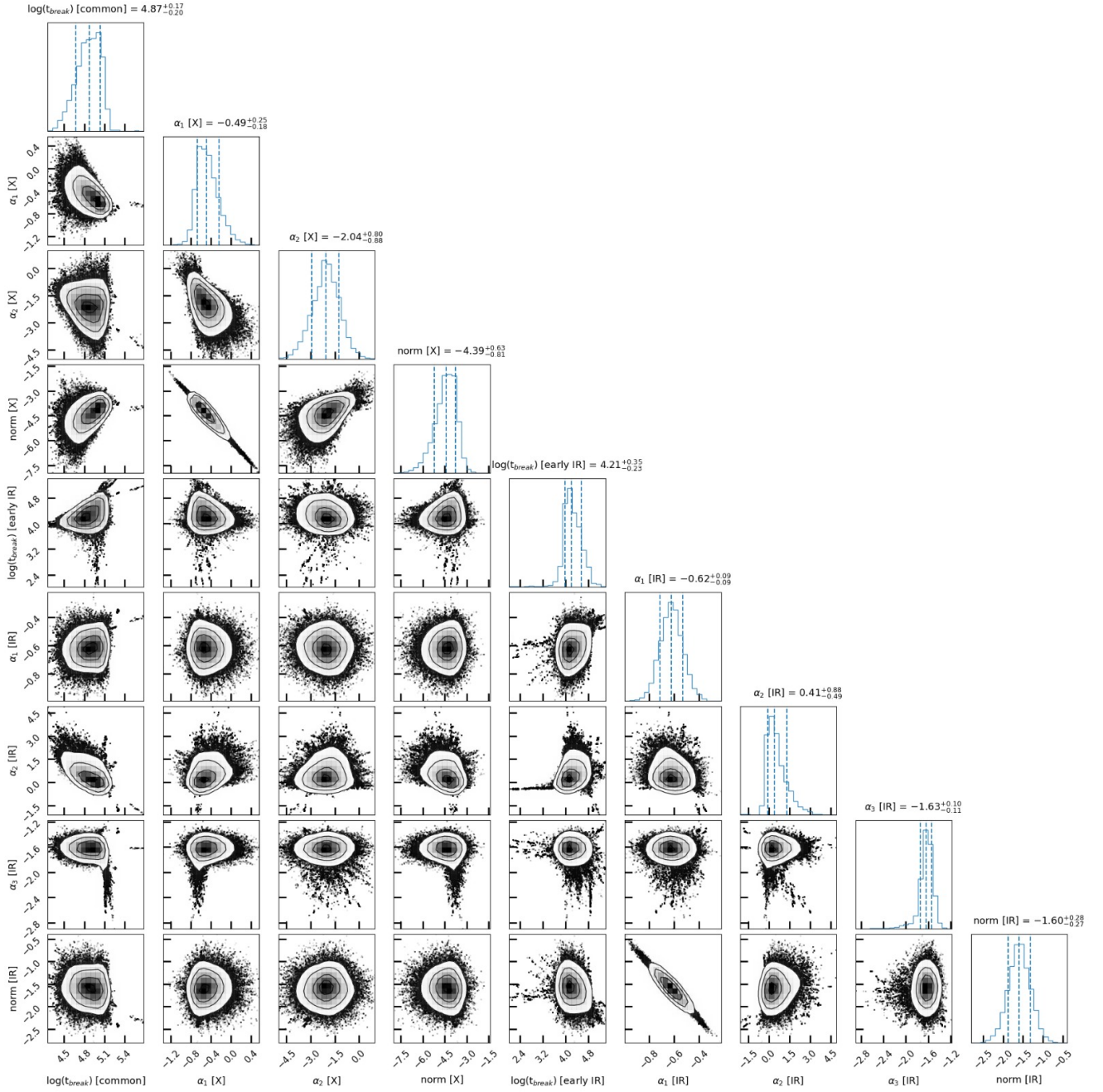


Fig. C.1. Posterior distributions of the combined fit of the X-ray and NIR light curves with double and single broken power law models, respectively. The X-ray break time and the second NIR break time were fitted as a single common parameter. The $\log(t_{\text{break}})$ values are reported in seconds, the normalisation parameter is in Jansky.

Appendix D: Contour plot for broadband fit with top-hat jet

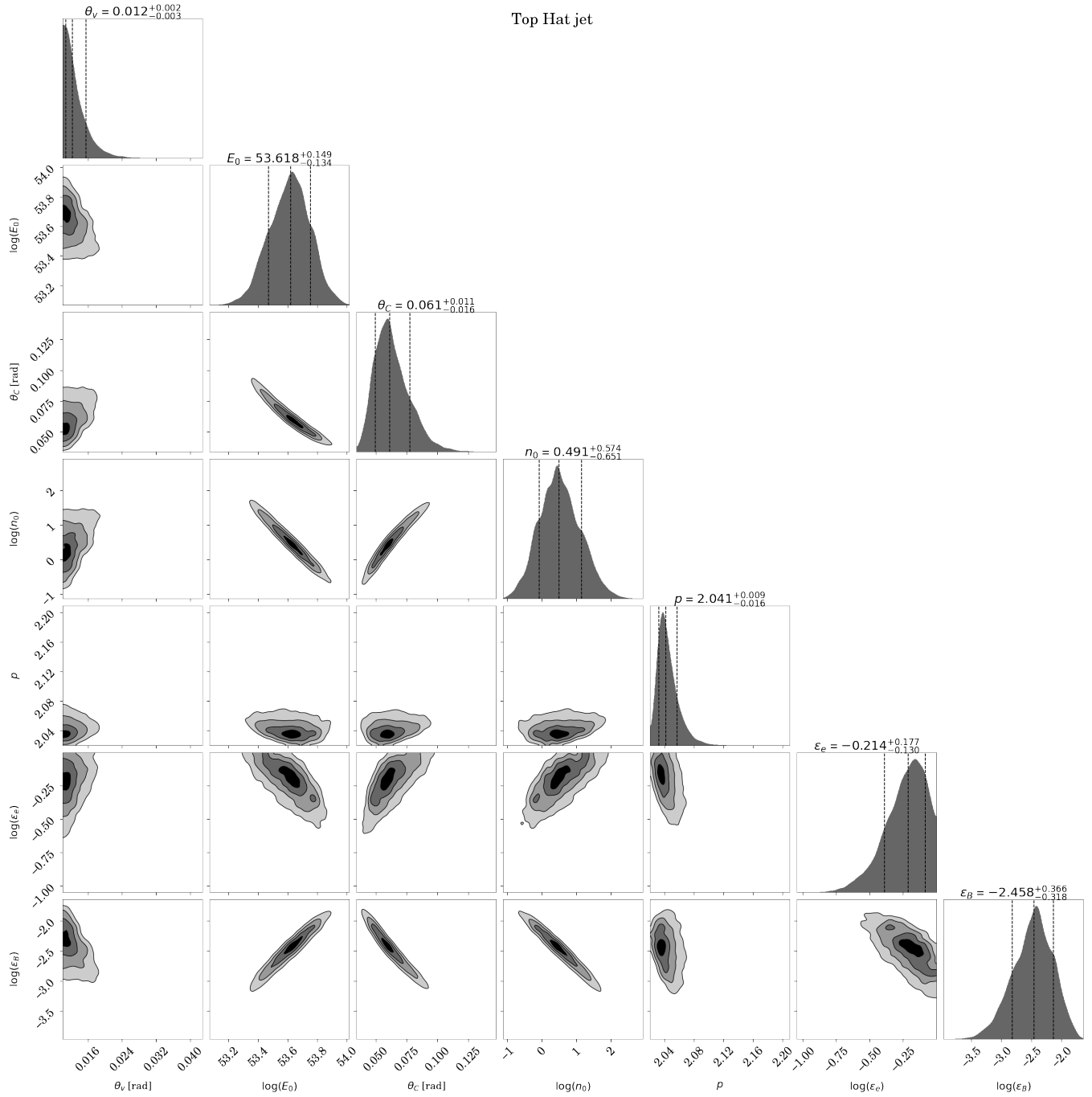


Fig. D.1. Corner plot for the top-hat jet fit of the X-ray, NIR, and radio light curves.

Appendix E: Contour plot for broadband fit with Gaussian jet

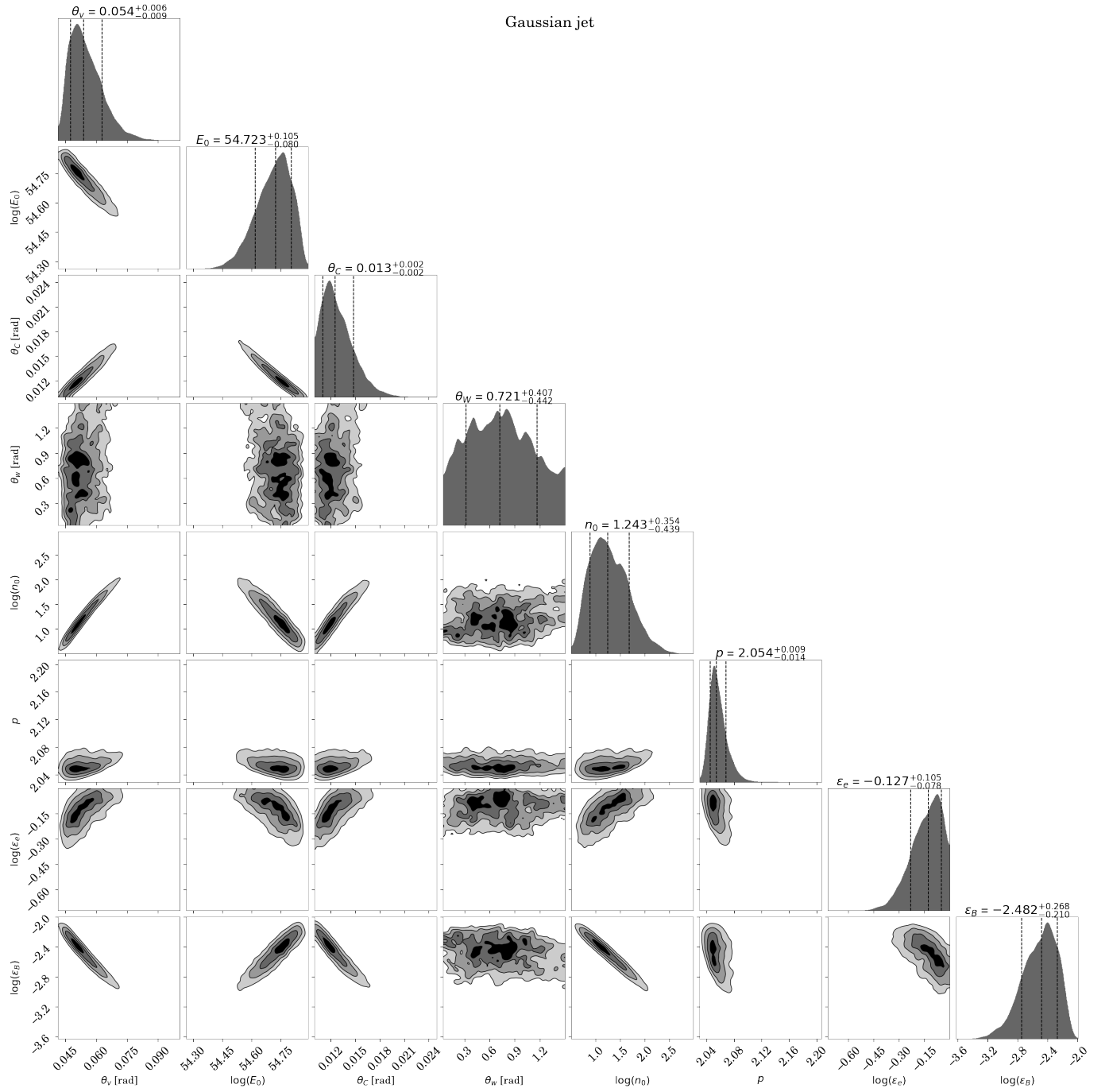


Fig. E.1. Corner plot for the Gaussian spreading jet fit of the X-ray, NIR, and radio light curves.

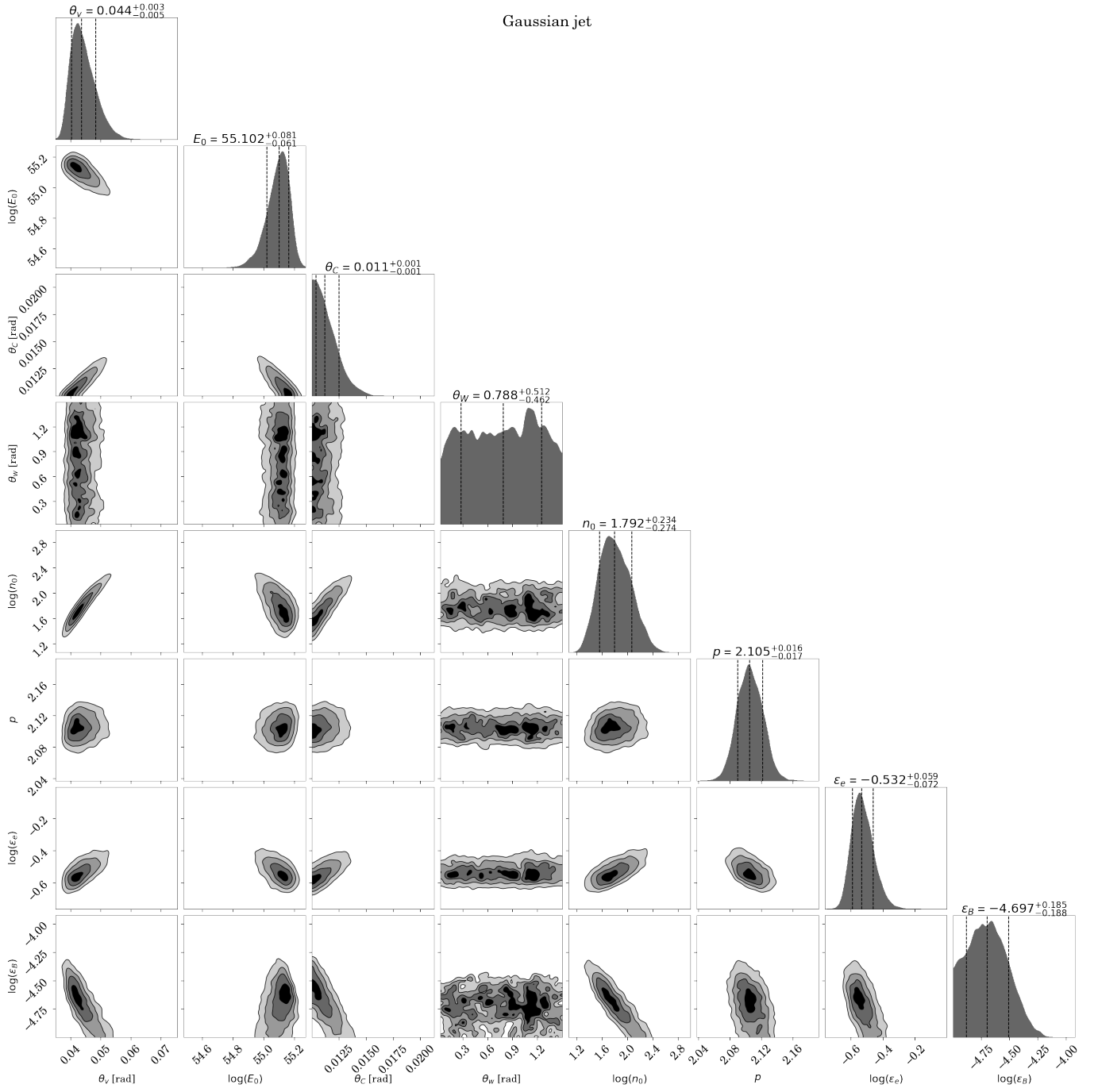


Fig. E.2. Corner plot for the Gaussian jet fit, without jet spreading, of the X-ray, NIR, and radio light curves.